Journal of Non-Newtonian Fluid Mechanics 349 (2026) 105569

Contents lists available at ScienceDirect

Journal of Non-Newtonian Fluid Mechanics

journal homepage: www.elsevier.com/locate/jnnfm

Full length article

A quasi-analytical solution for Carreau–Yasuda-type shear-thinning flows in slightly tapered pipes using a truncated power-law model

Gianluca Santesarti [a,b,*], Michele Marino [a], Francesco Viola [c], Roberto Verzicco [c,d,e], Giuseppe Vairo [a,f]

[a] University of Rome Tor Vergata, Department of Civil Engineering and Computer Science Engineering, 00133 Rome, Italy
[b] Sapienza University of Rome, Department of Mechanical and Aerospace Engineering, 00184 Rome, Italy
[c] Gran Sasso Science Institute, L'Aquila, 67100, Italy
[d] University of Rome Tor Vergata, Department of Industrial Engineering, 00133 Rome, Italy
[e] Physics of Fluids Group, Max Planck Center for Complex Fluid Dynamics, MESA+ Institute and J. M. Burgers Centre for Fluid Dynamics, University of Twente, P.O. Box 217, 7500AE Enschede, Netherlands
[f] University of Brasília, Department of Mechanical Engineering, Campus Darcy Ribeiro, Asa Norte, 70910-900 Brasília, DF, Brazil

ARTICLE INFO

Keywords:
Non-Newtonian shear-thinning fluids
Polymeric internal flows
Carreau–Yasuda flows
Lubrication theory
Extrusion bioprinting

ABSTRACT

This paper presents a quasi-analytical framework for shear-thinning generalized Newtonian fluids flowing in slightly tapered conical pipes. The nonlinear rheology is approximated through a Truncated Power-Law (TPL) formulation, characterized by Newtonian plateaus at low and high shear rates connected by a finite power-law region. Relying on lubrication theory and the slender approximation, a quasi-analytical solution is derived for velocity, pressure gradient, and shear stress distributions. The solution strategy is validated against dedicated numerical simulations, showing excellent agreement and confirming both consistency and predictive accuracy. An application to extrusion-based bioprinting illustrates how the framework can be employed to evaluate shear stresses in conical nozzles, identify critical operating conditions, and support process optimization, thus reducing reliance on costly simulations and trial-and-error experiments. The MATLAB scripts used for the flow solutions have been made available for the community use.

1. Introduction

Flows in tapered pipes (i.e., channels whose cross-sectional dimensions vary gradually along the axial direction, such as conical ducts) are encountered in a wide range of research and industrial applications, including polymer processing [1,2], food engineering [3], and biomedical systems [4–8]. The mathematical modeling of such flows has been extensively investigated since the last century for both Newtonian and non-Newtonian fluids.

Focusing on Newtonian fluids and aiming to analyze boundary-layer separation mechanisms, Blasius [9] analyzed axisymmetric steady laminar flows in channels with a radius varying slowly and exponentially along the axial coordinate. Through an order-of-magnitude analysis and the method of successive approximations, he derived closed-form solutions for both the axial and radial velocity components. Later, Forrester and Young [8] explored the boundary layer separation of blood in vascular diseases, referring to slightly converging and diverging tubes to model mild stenosis and dilation conditions, respectively. They obtained a fourth-order polynomial solution for the axial velocity profile. Langlois [10] investigated creeping flows in conical tubes, deriving a closed-form solution via a power series expansion in the taper angle, under the assumption that streamlines are straight lines radiating from the cone vertex. In a similar context of viscous flows in mildly tapered and axisymmetric ducts, Kotorynski [11] developed a solution for both axial and radial velocity components using the recursive successive approximation method, expressing results as functions of the axial pressure gradient. Finally, adopting a perturbation analysis approach, Sisavath et al. [12] extended the analysis of Forrester and Young [8] by deriving an asymptotic solution of the Navier–Stokes equations at low Reynolds numbers for flows through constricted tubes with different values of constriction wavelength and amplitude.

However, in many advanced applications, the working fluids exhibit complex non-Newtonian and nonlinear rheological behavior [1]. In particular, reference is made to the class of generalized Newtonian fluids (GNFs), also known as viscous inelastic fluids, which display shear-thinning and viscoplastic effects [1]. For these fluids, shear

---

* Corresponding author at: University of Rome Tor Vergata, Department of Civil Engineering and Computer Science Engineering, 00133 Rome, Italy.
E-mail addresses: santesarti@ing.uniroma2.it (G. Santesarti), m.marino@ing.uniroma2.it (M. Marino), francesco.viola@gssi.it (F. Viola), verzicco@uniroma2.it (R. Verzicco), vairo@ing.uniroma2.it (G. Vairo).

https://doi.org/10.1016/j.jnnfm.2026.105569
Received 3 March 2025; Received in revised form 24 January 2026; Accepted 17 February 2026

stress depends on the instantaneous shear rate and can be described by a generalized constitutive equation analogous to that of Newtonian fluids, where the apparent (or effective) viscosity is a nonlinear decreasing function of the shear rate. A wide range of empirical constitutive models have been proposed in the literature, including the power-law model [13,14], the Casson model [15], the Bingham model [16], the Herschel–Bulkley model [17], the Carreau model [18], and the Carreau–Yasuda model [1,19]. Among these, the Carreau–Yasuda model is widely recognized as a robust and versatile framework for describing the shear-thinning behavior of complex fluids. It captures fluid responses characterized by weak apparent-viscosity variations in both low- and high-shear-rate regimes (corresponding to quasi-Newtonian behavior) while accurately representing the pronounced nonlinear transition observed in the intermediate shear-rate range [1,20]. This transition region is commonly referred to as the power-law region, as it can be accurately approximated by the Ostwald–de Waele power-law description [13,14]. Nevertheless, despite its extensive application in various fields, such as polymer processing [21], hemodynamics [22], bioprinting [23–25], lubricant engineering [26], and food technology [27], the Carreau–Yasuda model presents intrinsic challenges related to parameter identifiability, which may compromise its predictive robustness and reliability [28,29]. To overcome these limitations, a more consistent rheological formulation, referred to as the shear rate-based rheological model (SRB), has recently been proposed by Santesarti et al. [29].

Several studies have been conducted to investigate non-Newtonian shear-thinning flows in tapered pipes. Sutterby [30] proposed a specific rheological model and employed a numerical method to evaluate the flow rate–pressure drop relationship. Oka and Murata [31] derived general integral solutions for shear stress, velocity, and flow rate, under the assumption of negligible inertial effects. A comparative analysis of the flow rate–pressure drop relationship for Casson fluids in both conical and cylindrical vessels was presented by Walawender and Prasassarakich [32]. Building on the work of Oka and Murata, How et al. [33] applied their results to polyacrylamide solutions, with viscosity data fitted using the power-law model, to study blood pressure loss in arterial prostheses. More recently, Priyadharshini and Ponalagusamy [34] extended the solution proposed by Forrester and Young [8] in the context of vascular pathologies, modeling blood as a Herschel–Bulkley fluid and providing a solution for the axial velocity component. Panaseti et al. [35] analyzed the lubrication flow of a Herschel–Bulkley fluid in a symmetric channel with varying width using a semi-analytical approach, while Fusi et al. [36] proposed a semi-analytical solution for Bingham-like flows in pipes with variable cross-sections.

Specifically referring to the Carreau–Yasuda model, since the nonlinear nature of its rheological formulation [1], it does not allow for analytical solutions even addressing simple geometries such as cylindrical tubes or parallel plate channels [37,38]. Nevertheless, in the cases of simple straight channels (i.e., cylindrical tubes or parallel walls), alternative and accurate closed-form solutions have been successfully developed, particularly in the context of hydraulic fracturing, by describing the fluid behavior via a Truncated Power-Law (TPL) model [37–39]. In this case, the effective viscosity follows a power-law behavior within a finite shear-rate range, and is truncated to constant values below and above defined threshold limits, resulting in ideal Newtonian response for low and high shear rate levels.

Building on this strategy, that is by describing the nonlinear rheological behavior of shear-thinning GNFs through a TPL approximation, the present paper introduces a novel quasi-analytical solution for Carreau–Yasuda-type flows in slightly tapered conical pipes. The proposed approach relies on lubrication theory and exploits the slender approximation [1,2], which neglects inertial convective terms in the momentum balance equations. Comparisons with dedicated benchmarking numerical simulations confirm the consistency and accuracy of the proposed solution strategy in capturing shear-thinning flow features in slightly tapered conical geometries.

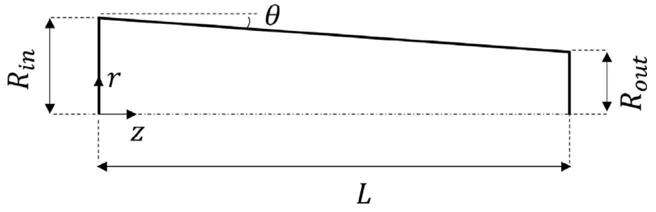

Fig. 1. Sketch and notation of the tapered axisymmetric conical pipe geometry addressed in the present study.

Finally, an application study illustrates how the proposed quasi-analytical framework can provide valuable insights to support optimization protocols in extrusion-based bioprinting processes, which often employ slightly tapered conical nozzles [4,40–44]. In such applications, the extruded non-Newtonian polymeric fluid (commonly referred to as bioink) contains living cells, whose viability is strongly influenced by the shear-stress distribution and can be preserved by properly tuning process parameters. The availability of an effective and accurate analytical tool thus has the potential to reduce time-consuming design phases that currently rely on computationally expensive simulations and/or trial-and-error experimental approaches.

2. Methods

2.1. Problem statement and general framework

Let a slightly tapered axisymmetric conical pipe be considered, characterized by the length L, inlet and outlet radii R_{in} and R_{out}, respectively, and the taper angle θ, assumed to be small. Accordingly, with reference to the notation introduced in Fig. 1, the following relationships hold:

$$\tan\theta = \frac{R_{out}}{L}\left(\frac{1-\chi}{\chi}\right) = \theta + o(\theta^2)\,, \tag{1}$$

$$R(z) = R_{in} - z\tan\theta \simeq R_{in} - z\,\theta\,, \tag{2}$$

where $\chi = R_{out}/R_{in} \leq 1$ is the tapering ratio.

An incompressible and homogeneous generalized Newtonian fluid, characterized by the density ρ, is assumed to flow inside the pipe. Consequently, the constitutive relationship between the deviatoric stress tensor $\boldsymbol{\tau}$ and the strain-rate tensor $\mathbf{E}$ reads [1]

$$\boldsymbol{\tau}(\dot{\gamma}) = 2\mu(\dot{\gamma})\,\mathbf{E} \ = \mu(\dot{\gamma})\ \left(\nabla\boldsymbol{v} + \nabla^T\boldsymbol{v}\right)\,, \tag{3}$$

where $\boldsymbol{v}$ is the fluid velocity, ∇ denotes the gradient operator, and $\mu(\dot{\gamma})$ is the effective viscosity depending on the scalar measure $\dot{\gamma}$ of the strain-rate tensor

$$\dot{\gamma} = \|2\mathbf{E}\| = \sqrt{2\mathrm{tr}\left(\mathbf{E}^T\mathbf{E}\right)} = \sqrt{2I_2}\,, \tag{4}$$

with I_2 being the second principal trace of the infinitesimal strain-rate tensor [1,45,46].

Since the problem axisymmetry, the flow can be conveniently described as bidimensional in the plane (r, z), with $r \in [0, R(z)]$ being the radial coordinate and $z \in [0, L]$ the axial one. Thereby, velocity and deviatoric stress fields can be represented as $\boldsymbol{v} = v_r\mathbf{e}_r + v_z\mathbf{e}_z$ and $\boldsymbol{\tau} = \tau_{rr}\mathbf{e}_r \otimes \mathbf{e}_r + \tau_{zr}(\mathbf{e}_r \otimes \mathbf{e}_z + \mathbf{e}_z \otimes \mathbf{e}_r) + \tau_{zz}\mathbf{e}_z \otimes \mathbf{e}_z + \tau_{\vartheta\vartheta}\mathbf{e}_\vartheta \otimes \mathbf{e}_\vartheta$, where $\mathbf{e}_r$ and $\mathbf{e}_z$ are the radial and axial directions, respectively, and $\mathbf{e}_\vartheta = \mathbf{e}_z \times \mathbf{e}_r$.

Consequently, by referring to a steady flow, the mass and momentum conservation equations result respectively in:

$$\frac{1}{r}\frac{\partial}{\partial r}(r v_r) + \frac{\partial v_z}{\partial z} = 0\,, \tag{5}$$

$$\text{along } \mathbf{e}_r : \quad \rho\left(v_r \frac{\partial v_r}{\partial r} + v_z \frac{\partial v_r}{\partial z}\right) = \left[\frac{1}{r}\frac{\partial}{\partial r}\left(r\tau_{rr}\right) + \frac{\partial \tau_{zr}}{\partial z} - \frac{\partial \tau_{\vartheta\vartheta}}{\partial r}\right] - \frac{\partial p}{\partial r}, \tag{6}$$

$$\text{along } \mathbf{e}_z : \quad \rho\left(v_r \frac{\partial v_z}{\partial r} + v_z \frac{\partial v_z}{\partial z}\right) = \left[\frac{1}{r}\frac{\partial}{\partial r}\left(r\tau_{zr}\right) + \frac{\partial \tau_{zz}}{\partial z}\right] - \frac{\partial p}{\partial z}, \tag{7}$$

completed by the following boundary conditions

$$\begin{array}{lll} \text{symmetry axis} & \dfrac{\partial v_z}{\partial r} = v_r = 0 & \text{at } r = 0, \\ \text{no-slip wall} & v_r = v_z = 0 & \text{at } r = R(z), \\ \text{outlet pressure} & p = 0 & \text{at } z = L. \end{array} \tag{8}$$

Addressing Carreau–Yasuda-type shear-thinning GNFs, the effective viscosity $\mu(\dot\gamma)$ introduced in Eq. (3) can be described by the SRB rheological model proposed in [29]

$$\mu(\dot\gamma) = \mu_0 \left[\frac{1 + \left(\lambda_\infty \dot\gamma\right)^a}{1 + \left(\lambda_0 \dot\gamma\right)^a}\right]^{\frac{(1-n)}{a}}, \tag{9}$$

where: μ_0 is the zero-shear rate viscosity, that is the viscosity value attained for $\dot\gamma \to 0^+$; a is the dimensionless strictly-positive Yasuda parameter [19], generally greater than one and regulating the transition between the Newtonian and power-law regions; n is a dimensionless strictly-positive model parameter that well approximates the power-law index regulating the rate of the viscosity change within the power-law region [29]; λ_0 and λ_∞ are two time constants (having the dimension of a time) delimiting the power-law region through the two characteristic shear rate levels $\dot\gamma_0 = 1/\lambda_0$ and $\dot\gamma_\infty = 1/\lambda_\infty$. Thereby, when $\lambda_\infty < \lambda_0$ and $a > 1$, a shear-thinning behavior is obtained if $n \in (0,1)$. The corresponding infinity-shear rate viscosity, that is the viscosity value attained for $\dot\gamma \to +\infty$, results in $\mu_\infty = \mu_0\left(\lambda_\infty/\lambda_0\right)^{1-n}$. It is worth observing that this description, when $\lambda_\infty \to 0^+$, recovers the classical Yasuda model [19], reproducing the rheological behavior of shear-thinning fluids exhibiting a quasi-Newtonian regime characterized by $\mu \simeq \mu_0$ for small shear rates (i.e., for $\dot\gamma < 1/\lambda_0$), followed by an indefinite shear-thinning behavior for any value of the shear rate greater than $1/\lambda_0$.

The rheological description in Eq. (9) can be conveniently approximated via a truncated power-law (TPL) approach [29,37], also referred to as a power-law-based piecewise approximation [29,38]. Specifically,

$$\mu(\dot\gamma) = \begin{cases} \mu_0 & \text{for } \dot\gamma \le 1/\lambda_0 \\ K\dot\gamma^{n-1} & \text{for } 1/\lambda_0 \le \dot\gamma \le 1/\lambda_\infty \\ \mu_\infty & \text{for } \dot\gamma \ge 1/\lambda_\infty \end{cases}, \tag{10}$$

where $K = \mu_0\lambda_0^{n-1} = \mu_\infty\lambda_\infty^{n-1}$ is the so-called consistency index (with $K > 0$) [1] of the classical power-law description [14]. Accordingly, the norm $\tau = \|\boldsymbol{\tau}\|$ of the deviatoric stress tensor in Eq. (3) results in:

$$\tau(\dot\gamma) = \mu(\dot\gamma)\,\dot\gamma = \begin{cases} \mu_0\dot\gamma & \text{for } \dot\gamma \le 1/\lambda_0 \\ K\dot\gamma^{n} & \text{for } 1/\lambda_0 \le \dot\gamma \le 1/\lambda_\infty \\ \mu_\infty\dot\gamma & \text{for } \dot\gamma \ge 1/\lambda_\infty \end{cases}, \tag{11}$$

with $\tau = \tau_0 = \mu_0\dot\gamma_0$ for $\dot\gamma \le 1/\lambda_0$ and $\tau = \tau_\infty = \mu_\infty\dot\gamma_\infty$ for $\dot\gamma \ge 1/\lambda_\infty$, where τ_0 and τ_∞ are denoted as the zero-shear stress and the infinity-shear stress, respectively.

As illustrated in the exemplary case shown in Fig. 2, the adopted TPL approach enables the approximation of the continuous viscosity profile described by Eq. (9) through a piecewise linear representation in the log–log $(\dot\gamma, \mu)$ space. This results in the straight identification of three distinct viscosity regimes: a low-shear Newtonian plateau with $\mu = \mu_0$ for $\dot\gamma \le \dot\gamma_0$, an intermediate power-law region for $\dot\gamma_0 \le \dot\gamma \le \dot\gamma_\infty$ characterized by the parameters K and n, and a high-shear Newtonian plateau with $\mu = \mu_\infty$ for $\dot\gamma \ge \dot\gamma_\infty$.

At the transition points (see Fig. 2)

$$X_0 = \left(\dot\gamma_0, \mu_0\right), \qquad X_\infty = \left(\dot\gamma_\infty, \mu_\infty\right), \tag{12}$$

viscosity continuity is satisfied. Similarly, the piecewise linear representation of the shear stress $\tau(\dot\gamma)$ in the log–log $(\dot\gamma, \tau)$ space ensures continuity at the corresponding points

$$Y_0 = \left(\dot\gamma_0, \tau_0\right), \qquad Y_\infty = \left(\dot\gamma_\infty, \tau_\infty\right). \tag{13}$$

To derive a quasi-analytical solution for a steady flow governed by the truncated power-law model within a slightly tapered axisymmetric conical channel, reference is made to the Newtonian and power-law solutions reported in Appendix A and Appendix B, respectively. These solutions are obtained from lubrication theory by order-of-magnitude analyses [1,2]. In particular, under the assumption of a slightly tapered channel (i.e., for small θ) and a low Reynolds number flow, both the inertial effects and radial component of the pressure gradient can be neglected. This simplification allows the axial component of the momentum balance equation in Eq. (7) to be expressed as follows (see Eqs. (A.4), (B.8))

$$\frac{\partial p(r,z)}{\partial z} \simeq p'(z) = \frac{1}{r}\frac{\partial\left(r\tau_{zr}\right)}{\partial r} = \frac{1}{r}\frac{\partial}{\partial r}\left(r\mu\frac{\partial v_z}{\partial r}\right), \tag{14}$$

so that the corresponding shear stress component τ_{zr} results in

$$\tau_{zr}(r,z) = p'(z)\frac{r}{2}, \tag{15}$$

where $p'(z) = dp(z)/dz$ denotes the axial pressure gradient. As a result, the scalar measures of the shear stress (τ) and strain rate ($\dot\gamma$) can be respectively computed as

$$\tau(r,z) \simeq |\tau_{rz}(r,z)|, \qquad \dot\gamma \simeq |\gamma_{zr}| \simeq \left|\frac{\partial v_z}{\partial r}\right|. \tag{16}$$

By integrating Eqs. (14) and (15) with respect to the radial coordinate r (that is, from the pipe axis at $r = 0$, to the wall at $r = R(z)$), the axial velocity profile $v_z(r,z)$ and the corresponding pressure gradient $p'(z)$ at each axial location $z \in [0, L]$ result in:

$$v_z(r,z) = -p'(z)\left[F(R(z),z) - F(r,z)\right], \tag{17}$$

$$p'(z) = \frac{4}{R^2(z)}\int_0^{R(z)} \tau_{zr}(r,z)\,dr, \tag{18}$$

where symmetry and no-slip boundary conditions are applied (see Eqs. (8)), and where

$$F(r,z) = \int_0^r \frac{\hat r}{2\mu\left(\dot\gamma(\hat r, z)\right)}\,d\hat r. \tag{19}$$

It is noteworthy that the expression of the axial velocity component in Eq. (17), derived for generalized Newtonian fluids, is formally analogous to the Darcy's law for Newtonian flow through porous media [47], given by $q = \sigma_{\text{hyd}}J$, where q is the specific flux, σ_{hyd} the hydraulic conductivity and $J = -p'(z)$ the hydraulic gradient. In this analogy, v_z corresponds to q, and the term $[F(R(z),z) - F(r,z)]$ plays the role of a equivalent hydraulic conductivity, which depends not only on the fluid viscosity and pipe geometry, but also on the operating conditions (e.g., flow rate), due to its dependence on the shear rate.

Finally, the radial velocity component $v_r(r,z)$ is derived directly from the mass conservation equation (5) as:

$$v_r(r,z) = -\frac{1}{r}\int r\frac{\partial v_z}{\partial z}\,dr + \frac{f(z)}{r} \tag{20}$$

where the function $f(z)$ is determined by imposing the symmetry condition at the pipe axis (see Eqs. (8)), and the continuity of the velocity field across the three viscosity regimes of the TPL approximation as detailed in the following.

2.2. Quasi-analytical solution

In order to derive an analytical solution for the problem under investigation, and referring to generalized Newtonian fluids described by the truncated power-law model introduced in Eq. (10), the main rationale can be summarized as follows.

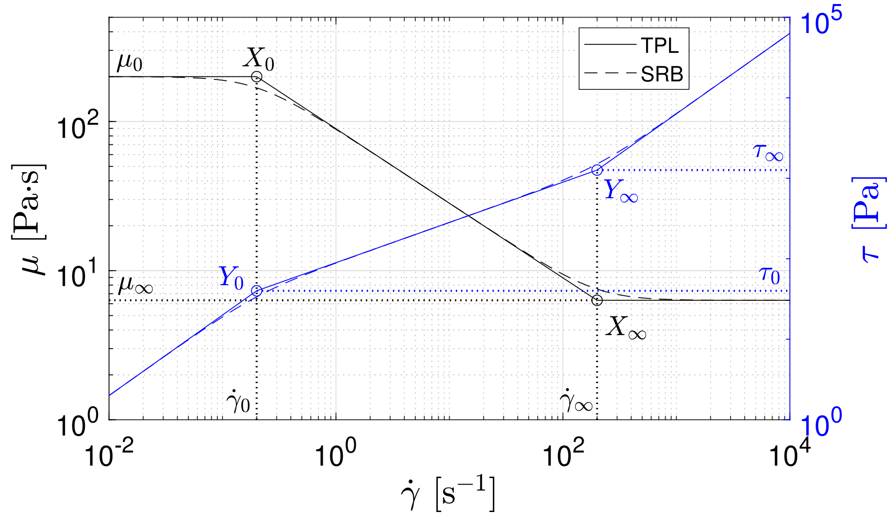

Fig. 2. Exemplary case of a shear-thinning response in GNFs. Viscosity μ (black lines, left axis) and deviatoric stress tensor norm τ (blue lines, right axis) vs. the shear rate $\dot\gamma$. Comparison between the SRB description (dashed line) and the TPL model (continuous line). Values of model parameters: $\mu_0 = 200$ Pa s, $\dot\gamma_0 = 1/\lambda_0 = 0.2$ s^{-1}, $\dot\gamma_\infty = 1/\lambda_\infty = 200$ s^{-1}, $n = 0.5$, $a = 2$. Consequently, $K = \mu_0 \lambda_0^{n-1} = 89.4$ Pa s$^{0.5}$, $\mu_\infty = \mu_0 \left(\lambda_\infty/\lambda_0\right)^{1-n} = 6.32$ Pa s, $\tau_0 = 40$ Pa, $\tau_\infty = 1264$ Pa.

Specifically, since the TPL model enables a clear distinction between Newtonian and power-law regimes depending on the local flow conditions, and since the flow regime is expected to vary smoothly within the channel with respect to both the axial coordinate z and the radial one r, it follows that, for a given cross-section (i.e., at a fixed value $z \in [0, L]$), either Newtonian or power-law behavior may arise depending on the radial position r. Accordingly, starting from Eq. (15), and for a given value of the axial pressure gradient $p'(z)$, one can introduce axially-dependent characteristic radii associated with the transitions through different rheological regimes, identified by the viscosity states in Eq. (12) (or equivalently by the stress states in Eq. (13)). These characteristic radii are defined as:

$$R_0(z) = -2\frac{\tau_0}{p'(z)}, \qquad R_\infty(z) = -2\frac{\tau_\infty}{p'(z)}, \tag{21}$$

where, since $p'(z)$ is expected negative for the problem under consideration, it results $0 < R_0(z) < R_\infty(z)$ in the case of a shear-thinning response. Therefore, $R_0(z)$ (respectively, $R_\infty(z)$) is the radius at which the magnitude of the shear stress is equal to the lower threshold $\tau_0 = \mu_0\dot\gamma_0$ (resp., the upper threshold $\tau_\infty = \mu_\infty\dot\gamma_\infty$). Accordingly, at a given axial location z and depending on the operating conditions (i.e., the flow rate Q and $\Delta p = p(0) - p(L)$), the pipe geometry (R_{in}, R_{out}, L and θ), and the rheological properties of the fluid (μ_0, λ_0, λ_∞, n and a), three main flow configurations can develop, as schematically represented in Fig. 3:

- $R(z) \le R_0(z)$ - The pipe cross-section is entirely characterized by a low-shear-rate (LSR) flow, where the fluid behaves as Newtonian with the high viscosity level μ_0 and the shear stress being such that $\tau(r, z) \le \tau_0$ for any $r \in [0, R(z)]$;
- $R_0(z) < R(z) \le R_\infty(z)$ - The pipe cross-section can be divided into two concentric flow regions: a LSR region for $r \le R_0(z)$, where the fluid behaves as Newtonian with the high viscosity level μ_0 and shear stress $\tau(r, z) \le \tau_0$; a medium-shear-rate (MSR) region for $R_0(z) < r \le R(z)$, where a power-law flow occurs, with $\mu_0 > \mu(\dot\gamma) > \mu_\infty$ and $\tau_0 < \tau(r, z) < \tau_\infty$;
- $R_\infty(z) < R(z)$ - The pipe cross-section can be divided into three concentric flow regions: a LSR region for $r \le R_0(z)$, where the fluid behaves as Newtonian with the high viscosity level μ_0 and shear stress $\tau(r, z) \le \tau_0$; a MSR region for $R_0(z) < r \le R_\infty(z)$, where a power-law flow occurs, with $\mu_0 > \mu(\dot\gamma) \ge \mu_\infty$ and $\tau_0 < \tau(r, z) \le \tau_\infty$; a high-shear-rate (HSR) region for $R_\infty(z) < r \le R(z)$, where the fluid behaves as Newtonian with the low viscosity level μ_∞ and shear stress $\tau(r, z) > \tau_\infty$.

Specifically, as $|p'(z)|$ (which is directly related to the pressure drop Δp along the pipe axis) increases, the characteristic radii $R_0(z)$ and $R_\infty(z)$ decrease, and the flow tends to exhibit a transition from the regime illustrated in Fig. 3(a) to that depicted in Fig. 3(c).

Following the solution strategy described in Appendices A and B, analytical relationships for velocity components (axial and radial), shear rate, and flow rate can be obtained as depending on the pressure gradient $p'(z)$. In detail, referring to the cases previously introduced, the following closed-form expressions result:

- $R(z) \le R_0(z)$: one-region configuration (LSR regime; Fig. 3(a))

$$v_{z,LSR}(r, z) = -\frac{p'(z)R^2(z)}{4\mu_0}\left[1 - \left(\frac{r}{R(z)}\right)^2\right], \tag{22a}$$

$$v_{r,LSR}(r, z) = -v_{z,LSR}(r, z)\,\frac{\theta}{R(z)}r, \tag{22b}$$

$$\dot\gamma_{zr,LSR}(r, z) = \frac{p'(z)}{2\mu_0}r, \tag{22c}$$

$$Q = Q_{LSR} = -\frac{p'(z)\pi R^4(z)}{8\mu_0}; \tag{22d}$$

- $R_0(z) < R(z) \le R_\infty(z)$: two-region configuration (Fig. 3(b))
  - For $r \le R_0(z)$ (LSR regime):

$$v_{z,LSR}(r, z) = A_0(z) + \frac{p'(z)}{4\mu_0}r^2, \tag{23a}$$

$$v_{r,LSR}(r, z) = -\frac{r}{2}\left[A_0'(z) + \frac{p''(z)}{8\mu_0}r^2\right], \tag{23b}$$

$$\dot\gamma_{zr,LSR}(r, z) = \frac{p'(z)}{2\mu_0}r, \tag{23c}$$

$$Q_{LSR} = \pi R_0^2(z)\left[A_0(z) + \frac{p'(z)R_0^2(z)}{8\mu_0}\right]; \tag{23d}$$

  - For $R_0(z) < r \le R(z)$ (MSR regime):

$$v_{z,MSR}(r, z) = \left[-\frac{p'(z)}{2K}\right]^{\frac{1}{n}}\frac{R(z)^\alpha - r^\alpha}{\alpha}, \tag{24a}$$

$$v_{r,MSR}(r, z) = -r\left[-\frac{p'(z)}{2K}\right]^{\frac{1}{n}}\left\{\frac{p''(z)}{p'(z)\alpha n}\left[\frac{R^\alpha(z)}{2} - \frac{r^\alpha}{\alpha+2}\right] - \frac{R^{\alpha-1}(z)}{2}\theta\right\} + \frac{f_0(z)}{r}, \tag{24b}$$

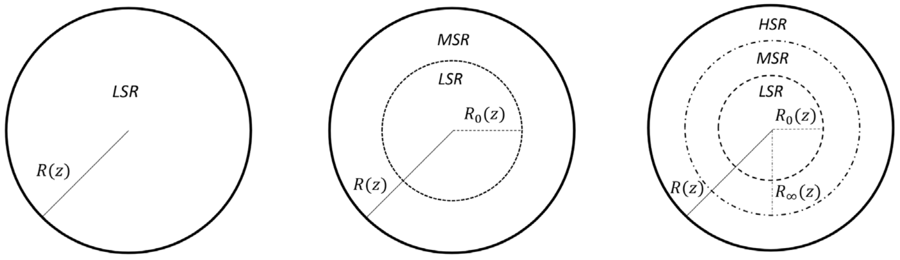

(a) (b) (c)

Fig. 3. Possible flow configurations in a channel cross-section under different flow regimes described by the TPL model, as defined through the characteristic radii in Eqs. (21). (a) $R(z) \le R_0(z)$: one-region configuration (LSR). (b) $R_0(z) < R(z) \le R_\infty(z)$: two-region configuration (LSR, MSR). (c) $R_\infty(z) < R(z)$: three-region configuration (LSR, MSR, HSR). LSR: low-shear-rate regime ($\dot{\gamma} \le 1/\lambda_0$); MSR: medium-shear-rate regime ($1/\lambda_0 < \dot{\gamma} \le 1/\lambda_\infty$); HSR: high-shear-rate regime ($\dot{\gamma} > 1/\lambda_\infty$).

$$\dot{\gamma}_{zr,MSR}(r,z) = -r^{\frac{1}{n}} \left[-\frac{p'(z)}{2K}\right]^{\frac{1}{n}} , \tag{24c}$$

$$Q_{MSR} = \frac{2\pi}{\alpha} \left[-\frac{p'(z)}{2K}\right]^{\frac{1}{n}} \left\{ \frac{R^\alpha(z)}{2} \left[R^2(z) - R_0^2(z)\right] - \frac{R^\beta(z) - R_0^\beta(z)}{\beta} \right\} ; \tag{24d}$$

$$Q = Q_{LSR} + Q_{MSR} ; \tag{25}$$

- $R_\infty(z) < R(z)$: three-region configuration (Fig. 3(c))
  - For $r \le R_0(z)$ (LSR regime): as in Eqs. (23);
  - For $R_0(z) < r \le R_\infty(z)$ (MSR regime):

$$v_{z,MSR}(r,z) = -\frac{r^\alpha}{\alpha} \left[-\frac{p'(z)}{2K}\right]^{\frac{1}{n}} + A_1(z) , \tag{26a}$$

$$v_{r,MSR}(r,z) = \frac{r^{\alpha+1}}{n\alpha\beta} \left[-\frac{p'(z)}{2K}\right]^{\frac{1}{n}} \frac{p''(z)}{p'(z)} - \frac{A_1'(z)}{2} r + \frac{f_0(z)}{r} , \tag{26b}$$

$$\dot{\gamma}_{zr,MSR}(r,z) = -r^{\frac{1}{n}} \left[-\frac{p'(z)}{2K}\right]^{\frac{1}{n}} , \tag{26c}$$

$$Q_{MSR} = A_1(z)\pi \left[R_\infty^2(z) - R_0^2(z)\right] - \frac{2\pi}{\alpha\beta} \left[-\frac{p'(z)}{2K}\right]^{\frac{1}{n}} \left[R_\infty^\beta(z) - R_0^\beta(z)\right] ; \tag{26d}$$

  - For $R_\infty(z) < r \le R(z)$ (HSR regime):

$$v_{z,HSR}(r,z) = -\frac{p'(z)}{4\mu_\infty} \left[R^2(z) - r^2\right] , \tag{27a}$$

$$v_{r,HSR}(r,z) = \frac{p''(z)}{16\mu_\infty} \left[2R^2(z) - r^2\right] r - \frac{p'(z)R(z)}{4\mu_\infty} r\theta + \frac{f_1(z)}{r} , \tag{27b}$$

$$\dot{\gamma}_{zr,HSR}(r,z) = \frac{p'(z)}{2\mu_\infty} r , \tag{27c}$$

$$Q_{HSR} = -\frac{p'(z)\pi}{8\mu_\infty} \left[R^2(z) - R_\infty^2(z)\right]^2 ; \tag{27d}$$

$$Q = Q_{LSR} + Q_{MSR} + Q_{HSR} ; \tag{28}$$

where $(\cdot)' = d(\cdot)/dz$, $\alpha = (n+1)/n$ and $\beta = (3n+1)/n$. The integration functions $A_0(z)$, $A_1(z)$, $f_0(z)$, and $f_1(z)$ are determined by prescribing continuity conditions of the velocity field across the interfaces defining the different flow subregions, that is at $r = R_0(z)$ and $r = R_\infty(z)$. More details are reported in Appendix C.

It is worth noting that the solution provided by Eqs. (22) to (28) depends on the axial pressure gradient $p'(z)$, which is not known a priori. In contrast to the Newtonian and power-law flow cases in slightly tapered conical channels (see Appendix A and Appendix B, respectively), the constitutive model based on the TPL formulation does not allow for a closed-form relationship between the flow rate Q and the pressure gradient $p'(z)$. To overcome this limitation, a semi-analytical iterative procedure has been developed and implemented numerically in the MATLAB environment (R2024b, MathWorks, MA, USA). For the sake of conciseness, further details are provided in Appendix D.

Finally, it is worth emphasizing that, when $\theta = 0$, the proposed approach reduces to the analytical solution for TPL-based flows in cylindrical ducts, characterized by a constant axial pressure gradient $p'(z) = -\Delta p/L$. Further details are provided in Appendix E.

2.3. Model validation against numerical benchmarks

In order to assess soundness and accuracy of the proposed approach, the quasi-analytical solution has been applied for the analysis of GNFs characterized by rheological properties within the range of typical non-Newtonian polymeric fluids employed in bioprinting applications. The corresponding results have been compared with numerical CFD simulations performed by considering both the SRB formulation in Eq. (9) and the corresponding TPL approximation in Eq. (10). To this aim, reference is made to a conical geometry defined by $R_{in} = 1.5$ mm, $R_{out} = 0.25$ mm, and $L = 20$ mm, corresponding to a taper angle of $\theta \simeq 3.58°$ (see Fig. 1) and a tapering ratio $\chi = R_{out}/R_{in} = 0.167$. These geometrical parameters are representative of conical nozzles commonly used in extrusion-based bioprinting [4,40–44]. The mean outflow velocity is set equal to $\bar{V}_{out} = 20$ mm/s, corresponding to a constant flow rate condition (with $Q = 3.93$ mm^3/s), which falls within the typical range adopted in bioprinting, namely $\bar{V}_{out} \le 40$ mm/s [4,43,48]. Two different sets of rheological parameters have been considered, as summarized in Table 1. They can be considered representative of non-Newtonian inelastic alginate-based bio-inks [49,50]. It is worth noting that the parameter set denoted as GNF A corresponds to a Carreau–Yasuda-type shear-thinning fluid, whereas GNF B is representative of a classical Yasuda response. The latter can be recovered through the SRB formulation (and thus through the TPL approximation) in the limiting case $\lambda_\infty \to 0^+$ (see Section 2.1). The flow is therefore characterized by a slenderness (or conicity) parameter [1] $R_{out}(1-\chi^2)/L = 1.22 \cdot 10^{-2}$, together with a maximum Reynolds number $Re_{(K,n)} = \rho V_z^{2-n} R_{out}^n / K = 8.33 \cdot 10^{-4}$ defined for a power-law fluid [51]. The small values of both parameters confirm the validity of the lubrication approximation and the associated slender-geometry assumptions adopted in the present formulation (see Section 2.1 and Appendix A, B). It is worth noting that inertial effects can, in principle, be incorporated into lubrication-type models, as demonstrated in classical studies on inertia-modified lubrication flows [52,53]. Nevertheless, under the extrusion bioprinting conditions considered in this work, the very low Reynolds number indicates that inertial contributions are negligible.

Table 1
Values of primary (in agreement with the SRB model) and derived rheological parameters, representative of two different GNFs and adopted in validation analyses.

	Primary					Derived			
	μ_0 [Pa s]	λ_0 [s]	λ_∞ [s]	a [-]	n [-]	μ_∞ [Pa s]	$\dot{\gamma}_0$ [s^{-1}]	$\dot{\gamma}_\infty$ [s^{-1}]	K [Pa s^n]
GNF A	200.0	1.0	0.05	2.0	0.5	44.7	1.0	20.0	200.0
GNF B	200.0	1.0	0.0	2.0	0.2	0.0	1.0	$+\infty$	200.0

Regarding the numerical software used, the flow through conical ducts is simulated using the commercial CFD ANSYS Fluent finite-volume solver (Release 2023 R2, Ansys Inc., Canonsburg, PA, USA). A steady, laminar, and axisymmetric flow problem is considered, governed by Eqs. (5) to (7) and referred to the bidimensional domain introduced in Fig. 1.

Convective fluxes are discretized through a second-order upwind scheme, viscous terms are treated by central differencing, and spatial gradients are evaluated using the least-squares cell-based method. Pressure–velocity coupling is numerically faced through the "coupled pressure-based" algorithm, which allows a robust and efficient single phase implementation for steady-state flows [54]. Specifically, the momentum and pressure correction equations are solved simultaneously within a single coupled system, ensuring an improved numerical stability, particularly for flows characterized by strong nonlinearities or high gradients. The shear-rate dependent viscosity laws (both SRB and TPL) were implemented into the ANSYS Fluent environment through user-defined functions (UDFs) using the "define_property" macro [55]. Within this framework, the apparent viscosity is locally evaluated at the cell level as a function of the instantaneous shear rate computed from the velocity-gradient tensor. The viscosity field is then updated at each global iteration and treated as a spatially varying material property during the solution of the momentum equations, consistently with the pressure-based solver formulation. The adopted computational mesh is defined by considering a structured topology and, as the result of a preliminary convergence analysis (herein omitted for the sake of brevity), consists of 37,500 quadrilateral cells (750 axial × 50 radial).

In agreement with Eqs. (8), a uniform pressure is prescribed at the outlet cross-section, while symmetry and no-slip boundary conditions are imposed at the nozzle axis and wall, respectively. At the inlet, starting from the assigned value of the flow rate Q, a power-law velocity profile defined via Eqs. (B.11) and (B.12) is imposed, such that the resulting mean velocity at the outlet $\bar{V}_{out} = Q/(\pi R_{out}^2)$ falls within the corresponding assigned value.

In order to reduce possible numerical artefacts induced by the imposed inlet and outlet boundary conditions, the computational domain was extended upstream and downstream of the conical nozzle depicted in Fig. 1 through the introduction of fictitious conical sections. A sensitivity analysis, omitted here for brevity, indicated that inlet and outlet axial extensions equal to $L/10$ provide an effective compromise between numerical accuracy and computational efficiency.

Numerical convergence was monitored by requiring the residuals of both the mass and momentum conservation equations to fall below 10^{-6}. Under these criteria, convergence was generally attained within approximately thirty iterations.

3. Results and discussions

3.1. Validation results: reference cases

By addressing to the reference geometry introduced in Section 2.3, results obtained through the proposed quasi-analytical (QA) solution based on the TPL formulation are compared in Figs. 4 (for rheological parameter set GNF A) and 5 (for GNF B) against the corresponding numerical results, computed using both the SRB and TPL models. The shear-thinning behaviors associated with the two parameter sets reported in Table 1 are shown in Figs. 4(a) and 5(a), where the TPL-based approximations closely match the SRB descriptions, with minor discrepancies occurring in the transition regions between quasi-Newtonian and power-law regions. Both cases analyzed are characterized by a mixed quasi-Newtonian and power-law flow regime along the nozzle axis as shown in Figs. 4(b) and 5(b), where the characteristic radii R_0 and R_∞, defined in Eqs. (21), are plotted versus the axial coordinate z and normalized with respect to local radius $R(z)$. Then, Figs. 4(c)–(f) and 5(c)–(f) report comparisons for the pressure distribution along the pipe axis (panels (c)) and the velocity fields (panels (d)–(f)).

As clearly shown, the TPL-based QA solution overlaps almost perfectly with the numerical CFD solution obtained via the TPL approximation, while also remaining very close to the SRB-based CFD results. This evidence confirms both the accuracy and robustness of the adopted strategy, as well as the soundness of the modeling assumptions underlying the lubrication theory.

More specifically, considering the solution for $p(z)$, the maximum percentage error (with respect to the SRB-based CFD results and observed at the inlet cross-section) is below 2.8% for GNF A and below 1% for GNF B. These very small discrepancies (fully negligible when the comparison is performed against the TPL-based CFD results) arise from the small differences between the two rheological descriptions (see Figs. 4(a) and 5(a)), in full agreement with previous findings on cylindrical Carreau–Yasuda flows [37,56,57].

Similar considerations hold for the velocity field. In detail, Figs. 4(d)–(f) and Figs. 5(d)–(f) show a very good agreement between quasi-analytical and numerical solutions, with the maximum discrepancy of about 4.4%, experienced for the outlet axial velocity component $v_z(r = 0, z = L)$ and for GNF B.

It is worth to highlight that the GNF B exhibits a more pronounced shear-thinning response than the GNF A (see Figs. 4(a) and 5(a)). As a consequence, the response predicted for the GNF B, compared against the GNF A case, results in:

- a pressure drop of about 6.5 times lower (see Figs. 4(c) and 5(c));
- an axial velocity component v_z characterized by smaller values at the duct axis and by a more uniform radial distribution (see Figs. 4(d)–(e) and 5(d)–(e));
- cross-sectional regions exhibiting a not-negligible radial velocity component v_r more shifted towards the pipe wall (see Figs. 4(f) and 5(f)).

Correspondingly, solutions associated to the GNF A and GNF B cases are expected to be characterized by different spatial distributions of the shear rate and therefore of the flow regime. To highlight how the flow regime evolves across each pipe cross-section, Figs. 4(a) and 5(a) report the working shear-rate window computed at the outlet section ($z = L$). This window is defined as the shear-rate range $[\dot{\gamma}_{0.05}, \dot{\gamma}_1]$, where $\dot{\gamma}_{0.05}$ (respectively, $\dot{\gamma}_1$) is the shear rate attained at the outlet radial coordinate r such that $r/R_{out} = 0.05$ (resp., $r/R_{out} = 1$). In detail, at $z = L$, the flow response of GNF A (resp., GNF B) shows a radial transition from a power-law regime near the nozzle axis (resp., Newtonian at $\mu = \mu_0$) to a Newtonian response at $\mu = \mu_\infty$ close to the nozzle wall (resp., power-law). As a direct consequence of the axial variability of the pressure gradient $p'(z)$ (see Figs. 4(c) and 5(c)), this transition mechanism is strongly dependent on the axial position z. Such an effect is clearly displayed in Figs. 4(b) and 5(b). In the GNF A case and for $0 \leq z/L \leq 0.65$, the pipe cross-section exhibits two shear-rate-based flow subregions: the LSR and the MSR, with the LSR progressively shrinking as z increases. For $z/L > 0.65$, an additional HSR annular subregion emerges, which rapidly expands with z. Conversely, for GNF B, since $R_\infty \to +\infty$ (as $\dot{\gamma}_\infty \to +\infty$), only the LSR and MSR subregions are present, with the MSR expanding as z increases.

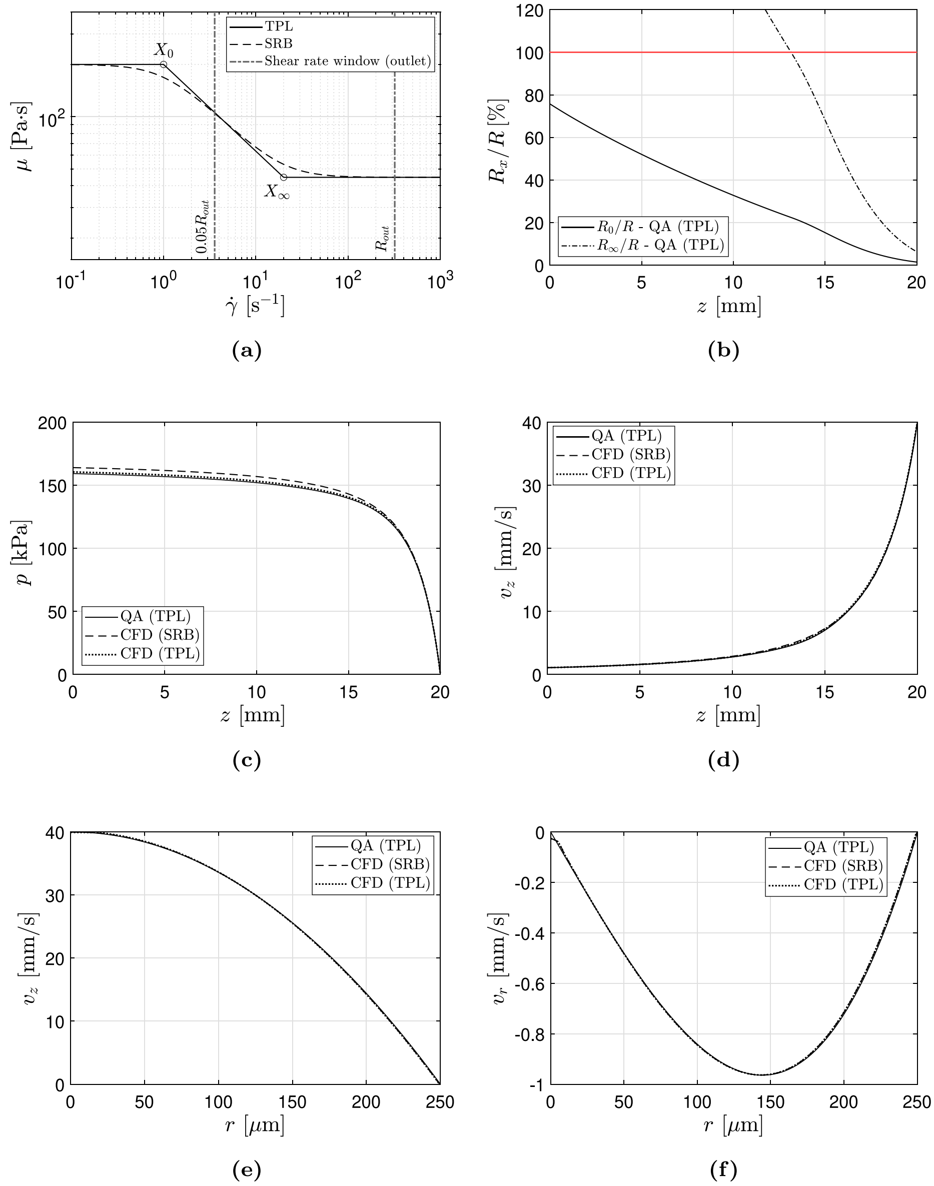

Fig. 4. Validation results for the reference geometry and GNF A (see Table 1). Comparison between quasi-analytical (QA) and numerical (CFD) solutions. (a) Viscosity μ vs. the shear rate $\dot{\gamma}$. (b) Normalized characteristic radii R_0 and R_∞ vs. the axial coordinate z. (c) Pressure p vs. the axial coordinate z. (d) Axial velocity component v_z at $r = 0$ vs. the axial coordinate z. (e) Axial velocity component v_z at the outlet ($z = L$) vs. the radial coordinate r. (f) Radial velocity component v_r at the outlet ($z = L$) vs. the radial coordinate r. SRB: shear rate-based rheological model. TPL: truncated power-law approximation.

3.2. Validation results: parametric analyses

To assess the accuracy limits of the proposed quasi-analytical approach, a campaign of parametric analyses was performed by varying, with respect to the reference cases previously discussed, the taper angle θ, the mean extrusion velocity $\bar{V}_{out}$ (i.e., the flow rate Q), and the fluid rheological properties.

3.2.1. Variation of the taper angle

Focusing on GNF A (see Table 1), the taper angle θ was varied in the range $[0, 10°]$. For consistency, the values of L, R_{out}, and Q were kept constant and equal to those adopted in the reference cases of Section 3.1. Quasi-analytical and numerical results are compared in Fig. 6, showing the distributions of the pressure $p(z)$ (panel (a)) and of the axial velocity at the nozzle centerline, $v_z(r = 0, z)$ (panel (b)). As clearly observed, although the discrepancies between the QA solution and the numerical results increase with θ, the proposed approach provides accurate predictions of both quantities even for almost non-negligible values of the taper angle. In particular, for $\theta = 10°$, the maximum percentage error remains below 8% with respect to the SRB-based CFD solution (6% with respect to the TPL-based CFD solution) for both pressure and velocity distributions. This finding is further confirmed in Fig. 6(c), where the percentage error $e_{\Delta p\%}$ in the predicted pressure drop Δp is reported as a function of θ.

Results for conical pipes also highlight a markedly different pressure–velocity coupling compared with the cylindrical case ($\theta = 0$), even for small taper angles. For instance, Fig. 6 shows that the inlet pressure decreases by more than 70% (and the inlet axial velocity by more than 80%) when θ increases from 0 to 1°. This demonstrates that, even for very small taper angles, cylindrical-pipe solutions are no longer accurate. This point is further supported by Fig. 6(d), where benchmark numerical solutions (for both rheological descriptions) are compared, under the same flow rate Q, with the TPL-based analytical solution

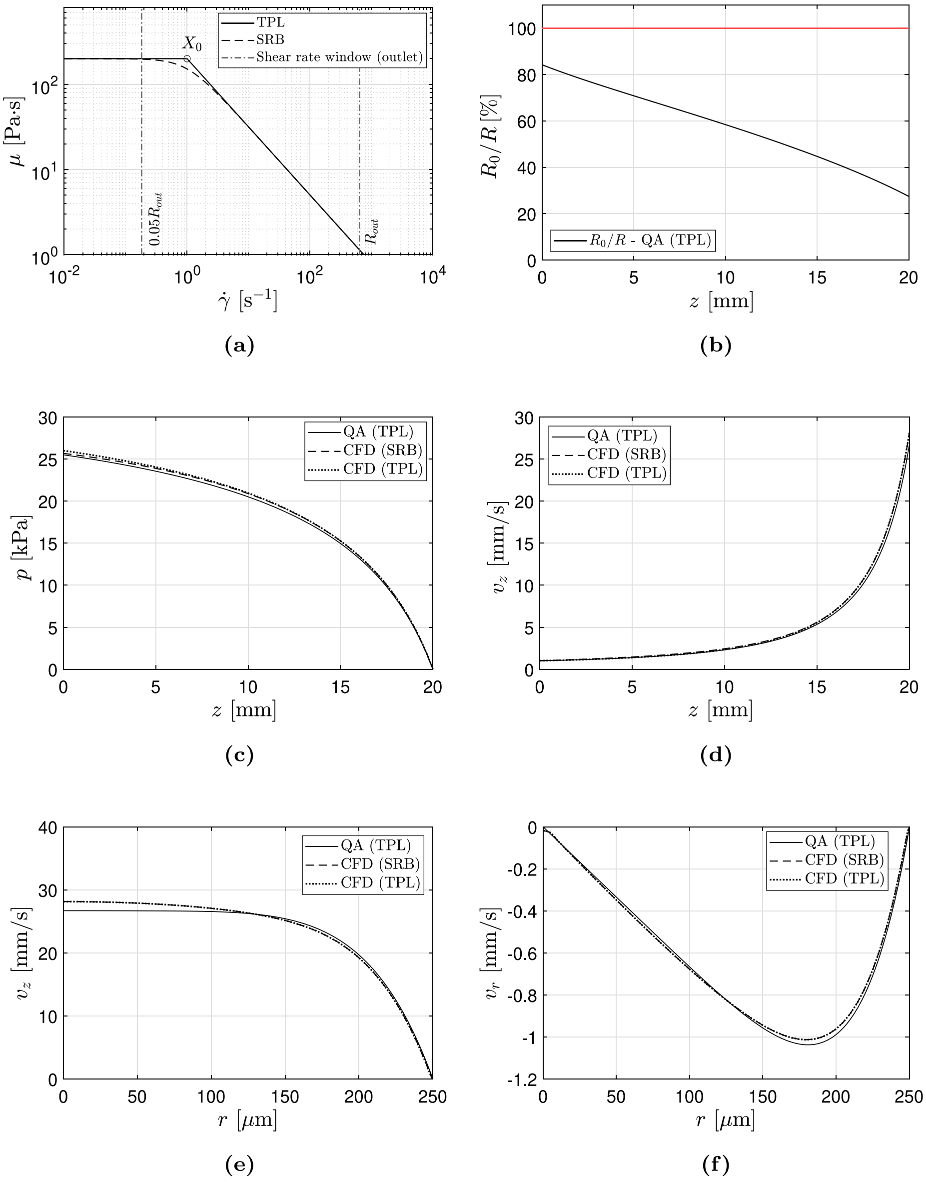

Fig. 5. Validation results for the reference geometry and GNF B (see Table 1). Comparison between quasi-analytical (QA) and numerical (CFD) solutions. (a) Viscosity μ vs. the shear rate $\dot{\gamma}$. (b) Normalized characteristic radius R_0 vs. the axial coordinate z. (c) Pressure p vs. the axial coordinate z. (d) Axial velocity component v_z at $r = 0$ vs. the axial coordinate z. (e) Axial velocity component v_z at the outlet ($z = L$) vs. the radial coordinate r. (f) Radial velocity component v_r at the outlet ($z = L$) vs. the radial coordinate r. SRB: shear rate-based rheological model. TPL: truncated power-law approximation.

valid for cylindrical flows [38,58,59]. The corresponding percentage error $e_{\Delta p\%}$, computed with respect to an equivalent cylindrical pipe (EQ-CYL) of length L and mean radius $\overline{R} = (R_{in} + R_{out})/2$, is already about 45% for $\theta = 1^\circ$ and rapidly approaches 90% for $\theta = 6^\circ$.

These results confirm that, even for very small taper angles, cylindrical-flow solutions cannot be applied reliably. Conversely, the proposed quasi-analytical approach remains consistent and accurate even for relatively large values of θ.

3.2.2. Variation of flow rate and fluid rheological properties

The analysis refers to the pipe geometry adopted in the reference cases (see Section 3.1) and to a Carreau–Yasuda-type shear-thinning fluid modeled through a TPL formulation. The flow rate Q was varied within the range $(0, 3.93]$ mm^3/s (corresponding to $0 < \bar{V}_{out} \leq 20$ mm/s), while the rheological properties of the fluid, with respect to GNF A in Table 1, were varied by ±30%.

For the sake of brevity, the TPL-based quasi-analytical results are compared with the numerical ones only in the worst-case scenario, namely against the SRB-based CFD solutions. In this case, the discrepancies reflect the combined effect of both the lubrication assumptions and the TPL approximation strategy.

The comparison is carried out on the axial velocity component at the outlet cross-section, by introducing the following error measure:

$$e^{out}_{v_z\%} = 100 \cdot \frac{2\pi \int_0^{R_{out}} |v_z^{(QA)}(r, L) - v_z^{(CFD)}(r, L)|\, r\, dr}{Q}, \tag{29}$$

which quantifies the mean percentage error associated with the outlet axial velocity profile. Its computation was performed through a dedicated post-processing routine developed in MATLAB (R2024b, MathWorks, Natick, MA, USA).

The corresponding results are summarized in Fig. 7. Specifically, the error measure remains below 3% in all cases (about 2.7% when varying n, and about 1.9% in the other cases). It is worth noting that, for all sets of rheological parameters, the maximum value of $e^{out}_{v_z\%}$ is attained at $\bar{V}_{out} \simeq 1.2$ mm/s (i.e., $Q \simeq 0.24$ mm^3/s). This behavior can be

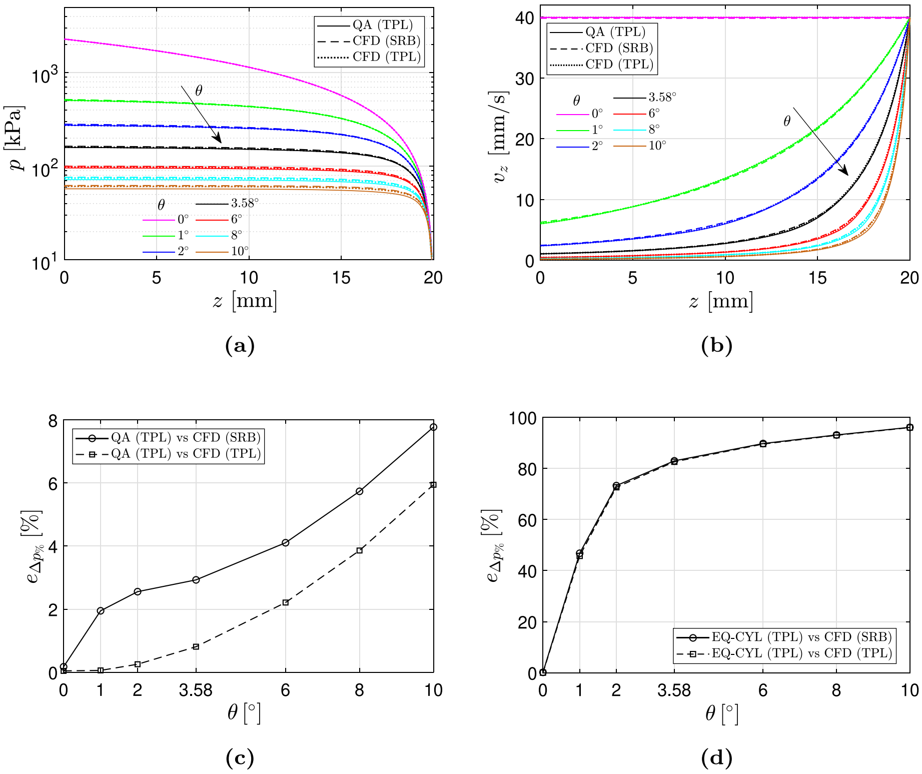

(a) (b)

(c) (d)

Fig. 6. Variation of the taper angle θ. Comparisons between quasi-analytical (QA) and numerical (CFD) solutions: (a) pressure p vs. the axial coordinate z; (b) axial velocity component v_z at $r = 0$ vs. the axial coordinate z; (c) pressure drop error $e_{\Delta p\%}$ vs. θ. (d) Pressure drop error $e_{\Delta p\%}$ between equivalent cylindrical solution (EQ-CYL) and CFD solutions vs. θ. SRB: shear rate-based rheological model. TPL: truncated power-law approximation.

attributed to the approximation of the fluid response through the truncated power-law model. As previously discussed, the TPL model shows some discrepancies with respect to the SRB rheological description in correspondence with the characteristic shear rates $\dot{\gamma}_0$ and $\dot{\gamma}_\infty$, where the constitutive transitions between quasi-Newtonian and power-law regimes occur (see Figs. 2 and 4(a)).

As a consequence, when Q increases, the flow regime at the outlet cross-section evolves from a two-region configuration (namely, LSR and MSR, Fig. 3(b)) to a three-region one (LSR, MSR, and HSR, Fig. 3(c)). In this case, the HSR subregion tends to extend at the expense of the other two, with the outlet shear-rate window (defined in Section 3.1) progressively covering the quasi-Newtonian regime at $\mu = \mu_\infty$, and thus becoming less sensitive to discrepancies at the transition shear rates. Accordingly, the maximum error occurs at a flow rate that induces an outlet shear-rate window encompassing both constitutive transitions and corresponds to an outlet cross-section characterized by a three-region regime with a significant extension of the MSR subregion.

3.3. *An application to extrusion-based bioprinting*

In practical extrusion-based bioprinting applications, the optimal setting of process variables is crucial to ensure compliance with specific functional requirements. However, this task is complicated by nonlinear couplings among the governing parameters [4,60] and often involves conflicting demands. For instance, a high mass flow rate is desirable to accelerate the printing process, but it typically induces high stress levels that may compromise cell viability [61,62]. Similarly, small-diameter nozzles enable high printing resolution but require higher extrusion pressures, which can negatively affect printability and increase the risk of cell damage [44,63,64].

To mitigate and control these effects, conical nozzles are often adopted. As also confirmed by the present results (Fig. 6(a)), for a given flow rate Q and outlet radius R_{out} (i.e., at fixed printing resolution and extrusion velocity $\bar{V}_{out}$), conical nozzles exhibit lower pressure drops compared to cylindrical ones [40–44]. Nevertheless, the identification of optimal process conditions in laboratory practice still relies predominantly on heuristic approaches, leading to demanding and time-consuming trial-and-error procedures, sometimes supported by complex computational modeling and numerical simulations [4,24,25]. These latter are also employed to quantify the stress distributions within the nozzle, with the aim of predicting and controlling potential cell damage. In particular, as in vascular flow studies [65,66], reference is generally made to shear stress distributions (expected to be maximum at the nozzle wall, see Eq. (15)), considered directly related to the onset and progression of cell damage [64,67,68].

Within this framework, the availability of an accurate and consistent analytical tool can provide valuable guidance for identifying and controlling optimal operating conditions. To demonstrate the potential impact of the proposed quasi-analytical solution, an exemplary application is presented in the following.

The case study concerns an extrusion process through a conical nozzle with the reference geometry introduced in Section 2.3. The bioink is modeled as a Carreau–Yasuda-like generalized Newtonian fluid with the following rheological properties: $\mu_0 = 200.0$ Pa s, $\lambda_0 = 5.0$ s, $\lambda_\infty = 0.01$ s, $a = 2.0$, $n = 0.5$ (corresponding to $\mu_\infty = 8.94$ Pa s, $\dot{\gamma}_0 = 0.2$ s^{-1}, $\dot{\gamma}_\infty = 100.0$ s^{-1}, $K = 89.4$ Pa s$^{0.5}$).

The direct application of the proposed quasi-analytical strategy, and in particular of Eqs. (22)–(28), enables a straightforward evaluation of the relationship between the mean extrusion velocity $\bar{V}_{out}$ and the pressure drop Δp, as shown in Fig. 8 (black curve). Furthermore, the approach makes it possible to monitor the shear-rate-based flow regimes within the nozzle, governed by the process variables Δp and $\bar{V}_{out}$, and directly linked to the corresponding shear stress distributions, which in turn play a crucial role in determining cell viability.

As an illustrative result, Fig. 8 shows (red curves) the variation of the characteristic radii R_0 and R_∞ (introduced in Eqs. (21)) at the

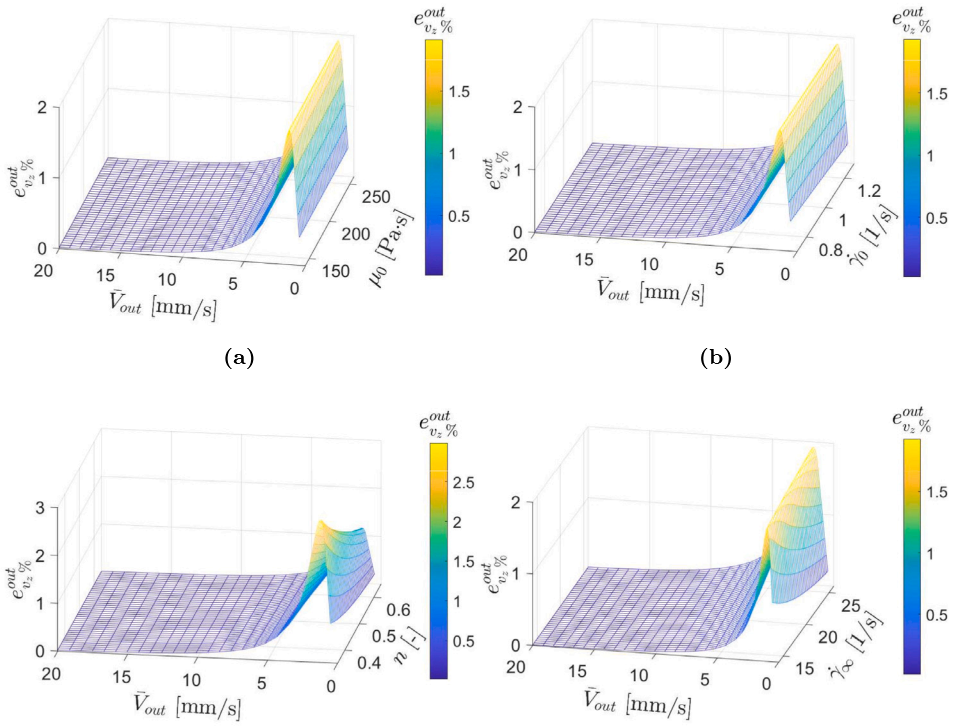

(a) (b)

(c) (d)

Fig. 7. Variation of flow rate and rheological properties. Comparisons between TPL-based quasi-analytical and SRB-based numerical solutions in terms of the error measure introduced in Eq. (29). Combined variation of $\bar V_{out}$ and (a) μ_0, (b) $\dot\gamma_0 = 1/\lambda_0$, (c) n, (d) $\dot\gamma_\infty = 1/\lambda_\infty$.

outlet cross-section as functions of Δp. At very low pressure drops, the flow rapidly exits the LSR regime, resulting in a dominant MSR up to $\bar V_{out} \simeq 5$ mm/s ($\Delta p \simeq 17$ kPa). For higher pressure drops (and thus larger mean extrusion velocities), an HSR regime emerges at the outlet in a near-wall annular subregion. This region quickly expands and becomes dominant (i.e., $R_\infty/R_{out} < 50\%$) when Δp exceeds approximately 30 kPa. In this regime, the flow tends toward a quasi-Newtonian behavior with $\mu \simeq \mu_\infty$, and the Δp-$\bar V_{out}$ relationship becomes nearly linear (see Fig. 8), consistent with Eq. (A.11). Conversely, for $\Delta p < 30$ kPa, the flow is mainly governed by a power-law response, leading to a nonlinear Δp-$\bar V_{out}$ coupling (see Fig. 8). Given the adopted rheological parameters (specifically, $n = 0.5$), this results in an almost quadratic Δp-$\bar V_{out}$ relationship, in agreement with Eq. (B.15).

The present approach also enables the direct evaluation of shear stresses within the nozzle and allows a parametric analysis of the influence of process variables (Δp and Q), nozzle geometry, and bio-ink rheology. In particular, it provides a means to control the process parameters so that shear stress levels remain below a critical threshold τ^* associated with cell damage onset. Specifically, cell viability requires that the maximum shear stress τ_{max} satisfies the inequality

$$\tau_{max} = \max_{z\in[0,L]}\left\{\frac{R(z)}{2}|p'(z)|\right\} = \frac{R_{out}}{2}|p'|_{out} \le \tau^* \qquad (30)$$

where, due to the slightly tapered conical geometry and the shear-thinning fluid response (see Fig. 2), the maximum shear stress occurs at the nozzle outlet (i.e., at $z = L$). Consequently, the safety condition can be rewritten as

$$|p'|_{out} \le \frac{2\tau^*}{R_{out}} \equiv |p'|^* \quad \Rightarrow \quad \bar V_{out} \le \bar V^*_{out} \equiv \frac{Q^*}{\pi R^2_{out}} \qquad (31)$$

where Q^* is the critical flow rate corresponding to $|p'|_{out} = |p'|^*$. Thus, for a given nozzle geometry and cell type, the critical operating variables (in particular $\bar V^*_{out}$) depend on the bio-ink rheological properties, which can therefore be considered as control parameters.

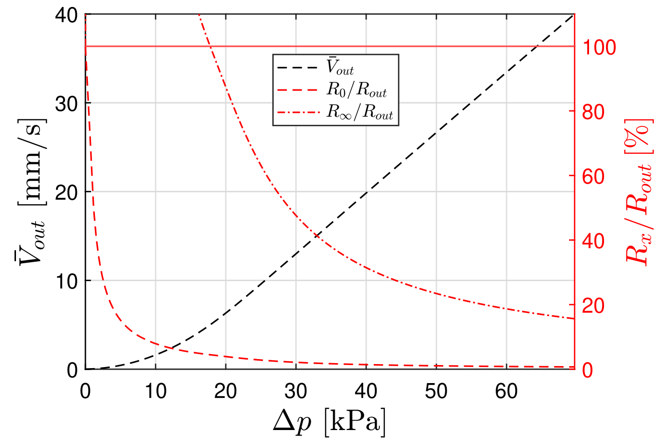

Fig. 8. Exemplary application to extrusion-based bioprinting. Mean extrusion velocity $\bar V_{out}$ vs. the nozzle pressure drop Δp (black line, left y-axis). Normalized characteristic radii R_0 and R_∞ at the outlet cross-section (red lines, right y-axis). Primary (and derived) rheological parameters: $\mu_0 = 200.0$ Pa s, $\lambda_0 = 5.0$ s, $\lambda_\infty = 0.01$ s, $a = 2.0$, $n = 0.5$ ($\mu_\infty = 8.94$ Pa s, $\dot\gamma_0 = 0.2$ s^{-1}, $\dot\gamma_\infty = 100.0$ s^{-1}, $K = 89.4$ Pa s$^{0.5}$).

For example, referring to the adopted nozzle geometry and allowing rheological properties to vary by ±75% with respect to those used in Fig. 8, Fig. 9 reports the critical extrusion velocity $\bar V^*_{out}$ for two values of the critical shear stress τ^*. Specifically, $\tau^* = 100$ Pa and $\tau^* = 500$ Pa are considered, which can be regarded as representative lower-bound thresholds for Schwann cells (RSC96) and myoblasts (L8) [44], and for rat adrenal medulla endothelial (RAMEC) cells [64], respectively, in alginate solutions. Notably, decreasing the zero-shear viscosity μ_0, the characteristic shear rate $\dot\gamma_0$, and the power-law index n, or increasing

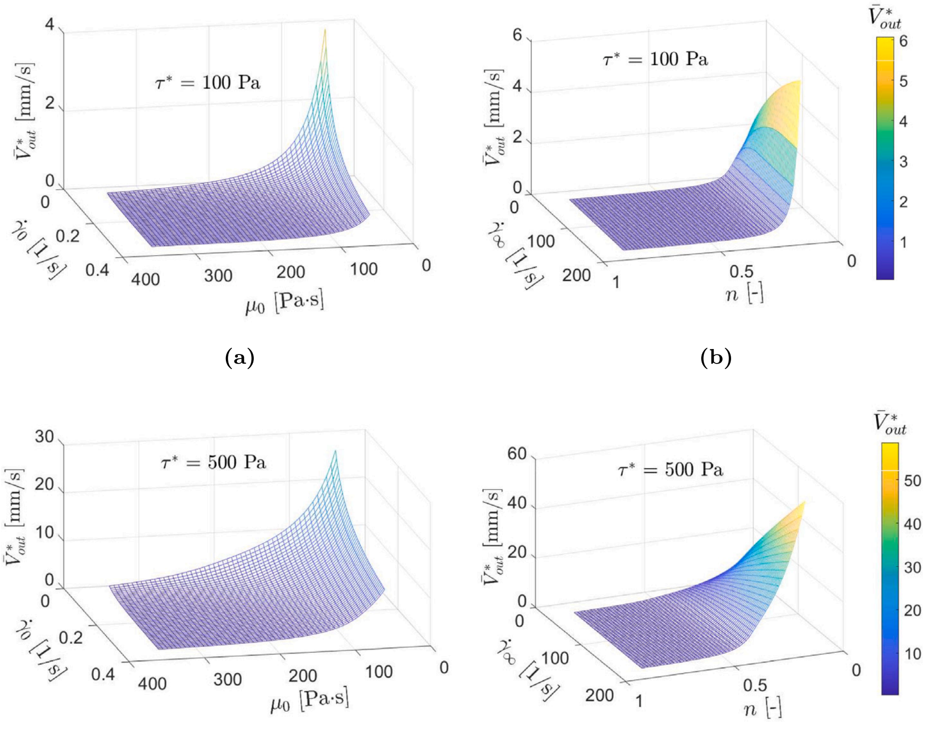

(a) (b)

(c) (d)

Fig. 9. Exemplary application to extrusion-based bioprinting. Critical extrusion velocity $\bar{V}^*_{out}$ inducing cell damage onset, for different levels of critical shear stress τ^* and by considering variations of rheological parameters with respect values adopted in Fig. 8. (a, $\tau^* = 100$ Pa), (c, $\tau^* = 500$ Pa) variation of μ_0 and $\dot{\gamma}_0$; (b, $\tau^* = 100$ Pa), (d, $\tau^* = 500$ Pa) variation of n and $\dot{\gamma}_\infty$.

the infinite-shear-rate $\dot{\gamma}_\infty$, shifts the critical extrusion velocity $\bar{V}^*_{out}$ to higher values. This behavior can be directly explained by the fact that these rheological variations promote the persistence of MSR regimes, delaying the onset of HSR. Finally, the results in Fig. 9 show that a fivefold increase in the critical shear stress τ^* can lead to up to a tenfold increase in $\bar{V}^*_{out}$.

4. Conclusions

In this work, a novel quasi-analytical solution based on lubrication theory has been presented for shear-thinning fluids with Carreau–Yasuda-like behavior flowing in slightly tapered conical pipes. The nonlinear constitutive relationship between viscosity and shear rate has been conveniently approximated through a truncated power-law (TPL) model, characterized by two Newtonian plateaus at low and high shear rates connected by a power-law region at intermediate shear rates. The proposed solution has been thoroughly validated against dedicated CFD-based numerical simulations, including a parametric analysis of the influence of geometrical and rheological variations. Results confirm the soundness and accuracy of the proposed analytical framework, showing that it remains reliable even for moderately large taper angles (e.g., the maximum error is below 8% for a taper angle of 10°). Additionally, a preliminary application to extrusion-based bioprinting demonstrates the potential of the approach to provide useful insights for the optimal setting of process parameters, as well as for identifying and controlling critical operating conditions affecting cell viability.

From an application standpoint, the developed quasi-analytical solution provides an effective and accurate tool that can reduce reliance on computationally expensive simulations or time-consuming experimental trial-and-error procedures, while offering quantitative guidance for process analysis and optimization across multiple fields. Potential applications include industrial polymer processing and biomedical systems involving shear-sensitive materials, with particular relevance to bioprinting technologies [4,24,25] and the modeling of cell-laden hydrogels [69,70], where predicting shear-thinning flows analytically can support the development and optimization of protocols to preserve cell viability and achieve precise deposition mechanisms. Moreover, the proposed solution strategy opens opportunities for advanced hemodynamic applications, such as establishing consistent analytical formulations to describe blood-vessel interactions in health and pathological tissue remodeling [71]. In addition, this framework could support the verification of new numerical approaches for GNFs.

Nevertheless, the proposed approach is subject to some inherent limitations. The main constraints are associated with the assumptions underlying the lubrication framework, whose validity depends on the magnitude of the relevant dimensionless parameters (namely the tapering ratio, the geometric slenderness of the nozzle, and the Reynolds number) and with the truncated power-law (TPL) approximation, which may not fully capture the transitions between quasi-Newtonian and strongly shear-thinning regimes, potentially underestimating extreme shear-rate-dependent behaviors outside the prescribed range. Furthermore, the truncated power-law approximation presents a continuous but non-differentiable behavior, which could affect the stability of the flow solutions. Future works may include the stability analysis of the flow solutions here presented, similarly as carried out in studies concerning the laminar-turbulent transition of Couette and Poiseuille plane flows with power-law fluids [72,73]. In addition, the validation of the solution here presented against fluid rheological parameters could be improved by performing the uncertainty quantification analysis as presented by Kim et al. [74] for flow predictions of other GNFs. Future extensions could also focus on incorporating more general constitutive models, addressing more complex geometries (e.g., tapered ducts with non-conical or non-axisymmetric shapes, possibly including branching), and considering transient flow conditions. These enhancements would further broaden the applicability of such a framework to complex bioprinting processes, industrial extrusion systems, and cardiovascular flows.

CRediT authorship contribution statement

Gianluca Santesarti: Writing – review & editing, Writing – original draft, Visualization, Software, Methodology, Data curation, Conceptualization. **Michele Marino:** Writing – review & editing, Supervision, Methodology, Conceptualization. **Francesco Viola:** Writing – review & editing, Supervision, Methodology, Conceptualization. **Roberto Verzicco:** Writing – review & editing, Supervision, Methodology, Conceptualization. **Giuseppe Vairo:** Writing – review & editing, Supervision, Methodology, Conceptualization.

Declaration of competing interest

The authors declare that they have no known competing financial interests or personal relationships that could have appeared to influence the work reported in this paper.

Acknowledgments

Part of this work was carried out with the support from the Italian National Group for Mathematical Physics GNFM-INdAM. Michele Marino and Giuseppe Vairo acknowledge financial support by the Italian Ministry of University and Research (MUR) under the National Recovery and Resilience Plan (NRRP), PRIN 2022 program, Project 2022T3SLAZ – CUP E53D23003700006. Francesco Viola acknowledges financial support by the European Research Council (ERC) under the European Unions Horizon Europe research and innovation program, Project CARDIOTRIALS – Grant No. 101039657. Gianluca Santesarti acknowledges financial support by Comune Fiuggi Young Project – ref. 3202SP-NILLOCSID.

Appendix A. Newtonian flow in a slightly tapered conical channel

In lubrication theory, it is common practice to estimate the relative magnitudes of the velocity components by introducing reference velocities, namely representative values of the velocity fields, in order to perform an order-of-magnitude analysis of the governing equations. This approach enables the identification of dominant terms and facilitates the simplification of the problem under specific physical assumptions.

For a Newtonian fluid with constant viscosity μ flowing in an axisymmetric tapered conical channel, the application of lubrication theory, combined with an order-of-magnitude analysis of the mass conservation equation [1,2], yields the following relationship between the reference axial velocity V_z and the radial one V_r:

$$V_r = V_z \frac{R_{out}}{L}\left(1-\chi^2\right), \tag{A.1}$$

where (see Fig. 1) R_{out} and R_{in} are the outlet and inlet radii of the duct, respectively, and $\chi = R_{out}/R_{in}$ denotes the corresponding tapering ratio.

Next, by considering the momentum conservation Eqs. (6) and (7) and performing an order-of-magnitude comparison between inertial and viscous terms, the following relationship is obtained:

$$\frac{O\,(\text{inertial terms})}{O\,(\text{viscous terms})} = Re\,\frac{R_{out}}{L}\left(1-\chi^2\right), \tag{A.2}$$

where the Reynolds number is defined as $Re = \rho V_z R_{out}/\mu$. Accordingly, for flows characterized by a low Reynolds number (i.e., creeping or Stokes flows), the above expression indicates that inertial terms are negligible compared to viscous terms. Moreover, the geometric factor $R_{out}(1-\chi^2)/L$ related to the taper angle θ further ensures the negligibility of inertial effects even in the presence of a slightly tapered channel geometry (i.e., for small θ) even when the Reynolds number is not strictly small. Hence, in these cases, the flow can be effectively treated as a fully laminar Stokes flow.

Similarly, comparing the components of the pressure gradient leads to:

$$\frac{O\left(\dfrac{\partial p}{\partial r}\right)}{O\left(\dfrac{\partial p}{\partial z}\right)} = \frac{R_{out}}{L}\left(1-\chi^2\right), \tag{A.3}$$

indicating that, in the case of a slightly tapered pipe, the radial component of the pressure gradient can also be neglected.

Consequently, the axial component of the momentum balance in Eq. (7) reduces to:

$$\frac{\partial p}{\partial z} \simeq p'(z) \simeq \frac{1}{r}\frac{\partial}{\partial r}\left(r\mu\frac{\partial v_z}{\partial r}\right) = \frac{\mu}{r}\frac{\partial}{\partial r}\left(r\frac{\partial v_z}{\partial r}\right), \tag{A.4}$$

which formally corresponds to the momentum balance equation for Newtonian flows in a cylindrical tube [1].

Integrating Eq. (A.4) along the radial direction r and applying symmetry and no-slip boundary conditions (see Eqs. (8)) the flow rate Q is obtained as:

$$Q = -\frac{\pi R^4(z)}{8\mu}p'(z) \tag{A.5}$$

which is formally equivalent to the Hagen–Poiseuille law for cylindrical flow, but incorporates the axial variation of the cross-sectional radius. This variation implies, in order to satisfy mass conservation, a corresponding axial variation in the pressure gradient.

Therefore, for a given flow rate Q, and considering the radius function $R(z)$ as defined in Eq. (1), the pressure distribution along the pipe axis is obtained as:

$$\begin{aligned} p(z) &= p_{in} - \frac{8}{3\pi}\frac{Q\mu}{\theta}\left[\frac{1}{(R_{in}-\theta z)^3} - \frac{1}{R_{in}^3}\right] \\ &= p_{in} - \frac{8Q\mu}{\pi R_{in}^4}z\left[1 + \frac{2\theta}{R_{in}}z + \sum_{m=3}^{\infty}\binom{-3}{m}\frac{(-1)^m}{3}\left(\frac{\theta}{R_{in}}z\right)^{m-1}\right], \end{aligned} \tag{A.6}$$

with p_{in} being the pressure value at the pipe inlet (i.e., at $z = 0$), and where the Taylor expansion around $\theta z/R_{in} = 0$ allows to highlight the effect induced by the tapered geometry with respect to the cylindrical case (the latter being recovered by setting $\theta = 0$).

Finally, by combining Eqs. (20), (A.4), and (A.5), the analytical expressions of the velocity components, shear rate, shear stress, and flow rate are obtained as follows:

$$v_z(r,z) = \frac{2Q}{\pi R^2(z)}\left[1-\left(\frac{r}{R(z)}\right)^2\right] = 2\bar{V}(z)\left[1-\left(\frac{r}{R(z)}\right)^2\right], \tag{A.7}$$

$$v_r(r,z) = -\frac{2Q}{\pi R^2(z)}\left[1-\left(\frac{r}{R(z)}\right)^2\right]\frac{\theta}{R(z)}r = -v_z(r,z)\frac{\theta}{R(z)}r, \tag{A.8}$$

$$\dot{\gamma}_{zr}(r,z) = -\frac{4Q}{\pi R^4(z)}r = -\frac{4\bar{V}(z)}{R^2(z)}r, \tag{A.9}$$

$$\tau_{zr}(r,z) = -\frac{4Q\mu}{\pi R^4(z)}r = -\frac{4\bar{V}(z)\mu}{R^2(z)}r, \tag{A.10}$$

$$\begin{aligned} Q &= -p'(z)\frac{\pi R^4(z)}{8\mu} = \frac{\Delta p}{L}\frac{3\pi}{8\mu}\frac{R_{in}^3 R_{out}^3}{\left(R_{in}^2 + R_{in}R_{out} + R_{out}^2\right)} \\ &= \frac{\Delta p}{L}\frac{\pi R_{in}^4}{8\mu}\left(1 - \frac{1+\chi+\chi^2-3\chi^3}{1+\chi+\chi^2}\right), \end{aligned} \tag{A.11}$$

where $\bar{V}(z)$ is the average axial velocity at the cross-section corresponding to a given $z \in [0, L]$, and $\Delta p = p(0) - p(L)$ denotes the total pressure drop along the pipe.

It is worth noting that the radial velocity component given in Eq. (A.8) is derived from the mass conservation condition in Eq. (20), by applying the symmetry condition at the pipe axis, $v_r(0,z) = 0$. Moreover, the distribution $v_r(r,z)$ vanishes in the case of a cylindrical pipe geometry, that is for $\theta = 0$.

Appendix B. Power-law flow in a slightly tapered conical channel

A strategy similar to that traced in Appendix A is adopted in the following, taking advantage from the lubrication theory and performing an order-of-magnitude analysis. The fluid response is assumed non-Newtonian and described by a power-law model [13,14], so that $\mu(\dot{\gamma}) = K\dot{\gamma}^{n-1}$ (see notation introduced in Eq. (10)).

Recalling that, for the problem under consideration (see Fig. 1 and Section 2.1) the strain rate tensor $\mathbf{E}$ results in

$$\begin{aligned}\mathbf{E} =& \frac{\partial v_r}{\partial r}\mathbf{e}_r \otimes \mathbf{e}_r + \frac{1}{2}\left(\frac{\partial v_r}{\partial z} + \frac{\partial v_z}{\partial r}\right)(\mathbf{e}_r \otimes \mathbf{e}_z + \mathbf{e}_z \otimes \mathbf{e}_r) \\ &+ \frac{v_r}{r}\mathbf{e}_\vartheta \otimes \mathbf{e}_\vartheta + \frac{\partial v_r}{\partial z}\mathbf{e}_z \otimes \mathbf{e}_z\,, \end{aligned} \tag{B.1}$$

an order-of-magnitude analysis leads to:

$$O\left(\frac{\partial v_r}{\partial r}\right) = O\left(\frac{v_r}{r}\right) = O\left(\frac{\partial v_r}{\partial z}\right) = O\left(\frac{V_z(1-\chi^2)}{L}\right) \tag{B.2}$$

$$O\left(\frac{\partial v_r}{\partial z} + \frac{\partial v_z}{\partial r}\right) = O\left(\frac{\partial v_z}{\partial r}\right) = O\left(\frac{V_z}{R_{out}}\right) \tag{B.3}$$

Accordingly, since Eq. (4), the components of the deviatoric stress tensor $\boldsymbol{\tau}$ satisfy the following order-of-magnitude conditions:

$$O(\tau_{rr}) = O(\tau_{\vartheta\vartheta}) = O(\tau_{zz}) = O\left(K\left(\frac{V_z}{R_{out}}\right)^n \frac{R_{out}(1-\chi^2)}{L}\right)\,, \tag{B.4}$$

$$O(\tau_{zr}) = O\left(K\left(\frac{V_z}{R_{out}}\right)^n\right)\,. \tag{B.5}$$

Thus, for slightly tapered conical geometries (that is, $\chi \to 1^-$) the strain rate tensor norm in Eq. (4) can be approximated as

$$\dot{\gamma} \simeq \left|\frac{\partial v_z}{\partial r}\right| \tag{B.6}$$

and the dominant deviatoric stress component is represented by τ_{zr}.

By considering the momentum conservation balance in Eqs. (6) and (7) and performing an order-of-magnitude comparison between inertial and viscous terms, the following relationship is obtained:

$$\frac{O\,(\text{inertial terms})}{O\,(\text{viscous terms})} = Re_{(K,n)}\frac{R_{out}}{L}\left(1-\chi^2\right)\,, \tag{B.7}$$

where $Re_{(K,n)} = \rho V_z^{2-n} R_{out}^n / K$ is the Reynolds number specified for a power-law fluid, as reported in [51]. The comparison of the pressure gradient components yields a relationship formally equivalent to that given in Eq. (A.3). Taking advantage of the same considerations stated in Appendix A for the case of Newtonian fluids, also for a power-law flow in a slightly tapered channel, the momentum balance equations can be recast by neglecting both the inertial terms and the radial pressure gradient. Accordingly, the axial component of the momentum balance in Eq. (7) reduces to:

$$\frac{\partial p}{\partial z} \simeq p'(z) \simeq \frac{1}{r}\frac{\partial}{\partial r}\left(rK\dot{\gamma}^{n-1}\frac{\partial v_z}{\partial r}\right)\,. \tag{B.8}$$

Integrating Eq. (B.8) along the radial direction r and applying symmetry and no-slip boundary conditions (see Eqs. (8)) the flow rate Q is obtained as:

$$Q = \left[-p'(z)\frac{1}{2K}\right]^{\frac{1}{n}} \frac{\pi R^\beta(z)}{\beta}\,, \tag{B.9}$$

where $\beta = (3n+1)/n$.

Therefore, for a given flow rate Q and considering the radius function $R(z)$ as defined in Eq. (1), the pressure distribution along the pipe axis is obtained as:

$$\begin{aligned} p(z) &= p_{in} - \left(\frac{Q\beta}{\pi}\right)^n \frac{2K}{3n\theta}\left[\frac{1}{(R_{in}-\theta z)^{3n}} - \frac{1}{R_{in}^{3n}}\right] \\ &= p_{in} - \left(\frac{Q\beta}{\pi}\right)^n \frac{2K}{R_{in}^{3n+1}} z \left[1 + \frac{(3n+1)\theta}{2R_{in}}z + \sum_{m=3}^{\infty}\binom{-3n}{m}\frac{(-1)^m}{3n}\left(\frac{\theta}{R_{in}}z\right)^{m-1}\right] \end{aligned} \tag{B.10}$$

where the Taylor expansion around $\theta z / R_{in} = 0$ allows to highlight the effect induced by the tapered geometry with respect to the cylindrical case (the latter being recovered by setting $\theta = 0$).

Finally, by combining Eqs. (20), (B.8), and (B.9), the analytical expressions of the velocity components, shear rate, shear stress, and flow rate are obtained as follows:

$$v_z(r,z) = \frac{\beta Q}{\alpha\pi R^2(z)}\left[1 - \left(\frac{r}{R(z)}\right)^\alpha\right] = \frac{\beta}{\alpha}\bar{V}(z)\left[1 - \left(\frac{r}{R(z)}\right)^\alpha\right]\,, \tag{B.11}$$

$$v_r(r,z) = -\frac{\beta Q}{\alpha\pi R^2(z)}\left[1 - \left(\frac{r}{R(z)}\right)^\alpha\right]\frac{\theta}{R(z)}r = -v_z(r,z)\frac{\theta}{R(z)}r\,, \tag{B.12}$$

$$\dot{\gamma}_{zr}(r,z) = -\frac{\beta Q}{\pi}\left[\frac{r}{R^{3n+1}(z)}\right]^{\frac{1}{n}} = -\beta\bar{V}(z)\left[\frac{r}{R^{n+1}(z)}\right]^{\frac{1}{n}}\,, \tag{B.13}$$

$$\tau_{zr}(r,z) = -\left(\frac{\beta Q}{\pi}\right)^n \frac{K}{R^{3n+1}(z)}r = -\left[\beta\bar{V}(z)\right]^n \frac{K}{R^{n+1}(z)}r\,, \tag{B.14}$$

$$\begin{aligned} Q &= \left[-p'(z)\frac{1}{2K}\right]^{\frac{1}{n}} \frac{\pi}{\beta}R^\beta(z) = \left(\frac{3n\,\Delta p}{2LK}\right)^{\frac{1}{n}} \frac{\pi}{\beta}\left(\frac{R_{in}-R_{out}}{\frac{1}{R_{out}^{3n}} - \frac{1}{R_{in}^{3n}}}\right)^{\frac{1}{n}} \\ &= \left(\frac{\Delta p}{2LK}\right)^{\frac{1}{n}} \frac{\pi R_{in}^\beta}{\beta}\left[1 - \frac{1-\chi^{3n} - 3n(1-\chi)\chi^{3n}}{1-\chi^{3n}}\right]\,, \end{aligned} \tag{B.15}$$

where $\alpha = (n+1)/n$, $\beta = (3n+1)/n$, $\bar{V}(z)$ is the average axial velocity at the cross-section corresponding to a given $z \in [0, L]$, and $\Delta p = p(0) - p(L)$ denotes the total pressure drop along the pipe.

As in the previous case (see Appendix A), the radial velocity component given in Eq. (B.12) is derived from the mass conservation condition in Eq. (20), by applying the symmetry condition at the pipe axis, $v_r(0,z) = 0$. Moreover, the distribution $v_r(r,z)$ vanishes in the case of a cylindrical pipe geometry, that is for $\theta = 0$.

Finally, it is interesting to note that the shear rate expression in Eq. (B.13), when evaluated at the pipe wall (i.e., for $r = R(z)$), coincides with the classical expression for the wall shear rate in a cylindrical duct, as reported in [75].

Appendix C. Integration functions $A_0(z)$, $A_1(z)$, $f_0(z)$, and $f_1(z)$

With reference to the notation and analytical solution provided in Section 2.2, the integration functions occurring in Eqs. (22) to (28) are determined by prescribing continuity conditions of the velocity field across the interfaces defining the different shear-rate dependent flow subregions, that is at $r = R_0(z)$ and $r = R_\infty(z)$. Specifically, they read as follows:

- $R_0(z) < R(z) \leq R_\infty(z)$: two-region configuration (LSR, MSR; Fig. 3(b))
  - For $r \leq R_0(z)$ (LSR regime):

$$A_0(z) = \left[-\frac{p'(z)}{2K}\right]^{\frac{1}{n}} \frac{\left[R^\alpha(z) - R_0^\alpha(z)\right]}{\alpha} - \frac{p'(z)R_0^2(z)}{4\mu_0}\,, \tag{C.1}$$

$$\begin{aligned} A_0'(z) =& \left[-\frac{p'(z)}{2K}\right]^{\frac{1}{n}} \left\{\frac{p''(z)}{p'(z)\alpha}\left[\frac{R^\alpha(z)}{n} + R_0^\alpha(z)\right] - \theta\,R^{\alpha-1}\right\} \\ &+ \frac{p''(z)R_0^2(z)}{4\mu_0}\,; \end{aligned} \tag{C.2}$$

  - For $R_0(z) < r \leq R(z)$ (MSR regime):

$$\begin{aligned} f_0(z) =& R_0^2(z)\left[-\frac{p'(z)}{2K}\right]^{\frac{1}{n}} \\ &\times \left\{\frac{p''(z)}{p'(z)\,n\,\alpha}\left[\frac{R^\alpha(z)}{2} - \frac{R_0^\alpha(z)}{\alpha+2}\right] - \frac{R^{\alpha-1}(z)}{2}\,\theta\right\} + R_0(z)\,v_{r,LSR}^{(0)}(z)\,; \end{aligned} \tag{C.3}$$

- $R_\infty(z) < R(z)$: three-region configuration (LSR, MSR, HSR; Fig. 3(c))

- For $r \leq R_0(z)$ (LSR regime):

$$A_0(z) = \left[-\frac{p'(z)}{2K}\right]^{\frac{1}{n}} \frac{\left[R_\infty^\alpha(z) - R_0^\alpha(z)\right]}{\alpha} - \frac{p'(z)}{4}\left[\frac{R_0^2(z)}{\mu_0} + \frac{R^2(z) - R_\infty^2(z)}{\mu_\infty}\right], \tag{C.4}$$

$$A_0'(z) = -\frac{p''(z)}{p'(z)}\left[-\frac{p'(z)}{2K}\right]^{\frac{1}{n}} \frac{\left[R_\infty^\alpha(z) - R_0^\alpha(z)\right]}{\alpha} + \frac{R(z)\,p'(z)}{2\mu_\infty}\,\theta - \frac{p''(z)}{4}\left[\frac{R^2(z) + R_\infty^2(z)}{\mu_\infty} - \frac{R_0^2(z)}{\mu_0}\right]; \tag{C.5}$$

- For $R_0(z) < r \leq R_\infty(z)$ (MSR regime):

$$A_1(z) = -\frac{p'(z)}{4\mu_\infty}\left[R^2(z) - R_\infty^2(z)\right] + \left[-\frac{p'(z)}{2K}\right]^{\frac{1}{n}} \frac{R_\infty^\alpha(z)}{\alpha}, \tag{C.6}$$

$$A_1'(z) = -\frac{p''(z)}{4\mu_\infty}\left[R_\infty(z)^2 + R^2(z)\right] + \frac{R(z)\,p'(z)}{2\mu_\infty}\,\theta - \frac{p''(z)}{p'(z)}\left[-\frac{p'(z)}{2K}\right]^{\frac{1}{n}} \frac{R_\infty^\alpha(z)}{\alpha}, \tag{C.7}$$

$$f_0(z) = R_0(z)\, v_{r,LSR}^{(0)}(z) - \frac{p''(z)}{p'(z)}\left[-\frac{p'(z)}{2K}\right]^{\frac{1}{n}} \frac{R_0^{\alpha+2}(z)}{n\,\alpha\,\beta} + \frac{A_1'(z) R_0^2(z)}{2}; \tag{C.8}$$

- For $R_\infty(z) < r \leq R(z)$ (HSR regime):

$$f_1(z) = R_\infty(z)\, v_{r,MSR}^{(\infty)}(z) - \frac{p''(z) R_\infty^2(z)}{16\mu_\infty}\left[2R^2(z) - R_\infty^2(z)\right] + p'(z)\frac{R_\infty^2(z)\,R(z)}{4\mu_\infty}\,\theta; \tag{C.9}$$

where $v_{r,LSR}^{(0)}(z) = v_{r,LSR}(R_0(z), z)$ and $v_{r,MSR}^{(\infty)}(z) = v_{r,MSR}(R_\infty(z), z)$.

Appendix D. Iterative procedure for determining the axial pressure gradient

As highlighted in Section 2.2, the TPL-based solution provided by Eqs. (22) to (28), despite the Newtonian and power-law flow cases, does not allow for a closed-form relationship between the flow rate Q and the axial pressure gradient $p'(z)$. Accordingly, a semi-analytical iterative procedure has been developed, based on the proposed Algorithm 1 and implemented numerically in the MATLAB environment (R2024b, MathWorks, MA, USA).

Let the conical pipe geometry, the flow rate Q, and the TPL-based rheological properties of the fluid be assigned, and let $p'_{\mu_0}(z)$, $p'_{\mu_\infty}(z)$ (computed via Eq. (A.5) by considering $\mu = \mu_0$ and $\mu = \mu_\infty$, respectively) and $p'_{(K,n)}(z)$ (computed via Eq. (B.9)) be the axial pressure gradients associated to Newtonian and power-law cases, respectively. Moreover, let the pipe conical domain be axially discretized into N conical subdomains, where the ith subdomain ($i = 1, \dots, N$) has an axial length $\Delta z_i = z_{i+1} - z_i$, with $z_1 = 0$ (inlet cross section) and $z_{N+1} = L$ (outlet cross section). As a notation rule, the pipe cross-section at z_i is denoted by Σ_i.

For each cross-section Σ_i, the value of the pressure gradient $p'_i \equiv p'(z_i)$ is computed by solving numerically the flow-rate conservation equation $\hat{Q}_i(p'_i) = Q$, where $\hat{Q}_i$ denotes the flow rate through Σ_i associated to the solution provided by Eqs. (22) to (28). It depends on p'_i itself, that in turn depends in a coupled way by the specific partition of Σ_i associated to the occurrence of different shear-rate regimes (namely, LSR, MSR, and HSR). Consequently, an iterative root-finding procedure is necessary. To this aim, the built-in MATLAB function *fzero*, based on a combination of bisection, secant, and inverse quadratic interpolation methods, is employed.

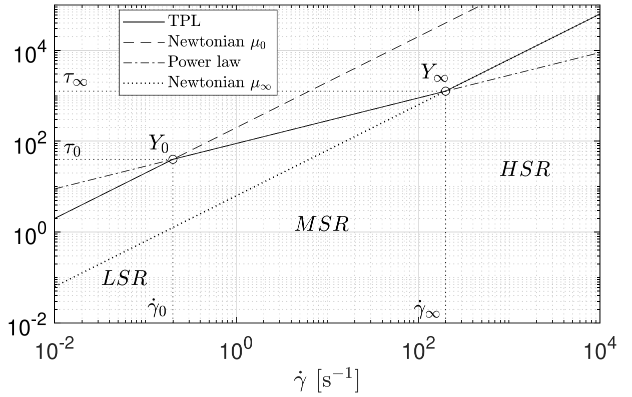

Fig. D.10. Exemplary case of the shear stress $\tau(\dot{\gamma})$ associated to the TPL model (continuous line). The corresponding Newtonian and power-law sub-cases (dashed and dotted lines) are also reported, highlighting the corresponding shear-rate regimes (LSR, MSR and HSR). Values of model parameters: $\mu_0 = 200$ Pa s, $\dot{\gamma}_0 = 1/\lambda_0 = 0.2$ s^{-1}, $\tau_0 = 40$ Pa, $\dot{\gamma}_\infty = 1/\lambda_\infty = 200$ s^{-1}, $n = 0.5$, $K = 89.4$ Pa s$^{0.5}$, $\mu_\infty = 6.32$ Pa s, $\tau_\infty = 1264$ Pa.

In the framework of the adopted TPL constitutive model, the identification of cross-sectional regions characterized by different flow regimes is carried out based on the characteristic radii R_0 and R_∞, defined in Eqs. (21). Consistent with the considerations introduced in Section 2.2, this procedure is equivalent to comparing, for each cross section Σ_i, the wall shear stress $\tau_w(z_i) = |p'_i|\,R(z_i)/2$ with the reference values $\tau_0 = \mu_0\dot{\gamma}_0$ and $\tau_\infty = \mu_\infty\dot{\gamma}_\infty$. Specifically, according to Eq. (18) and referring to the illustrative case depicted in Fig. D.10, the following relationships hold

$$\begin{aligned} &|p'_i|\,R(z_i)/2 \leq \tau_0 && \Rightarrow \quad \hat{Q}_i = Q_{LSR}(z_i) \\ &\tau_0 < |p'_i|\,R(z_i)/2 \leq \tau_\infty && \Rightarrow \quad \hat{Q}_i = Q_{LSR}(z_i) + Q_{MSR}(z_i) \\ &|p'_i|\,R(z_i)/2 > \tau_\infty && \Rightarrow \quad \hat{Q}_i = Q_{LSR}(z_i) + Q_{MSR}(z_i) + Q_{HSR}(z_i) \end{aligned} \tag{D.1}$$

Since $|p'(z)|$ is expected monotonically increasing with z, when a suitably fine axial discretization is considered (namely, for a suitable choice of N), it is possible to assume that $1 \leq n_{SR}(\Sigma_i) \leq n_{SR}(\Sigma_{i-1}) + 1 \leq 3$, where $n_{SR}(\Sigma_i)$ is the number of the shear-rate regimes at Σ_i. Moreover, the converged solution p'_{i-1} at Σ_{i-1} is assigned as the first guess value p'_{i*} for the iteration procedure at Σ_i, except for the inlet section Σ_1. For this latter, the first guess value p'_{1*} is assigned as depending on the quantity $|p'_1|_{min} \equiv \min\left\{\left|p'_{\mu_0}(z_1)\right|, \left|p'_{(K,n)}(z_1)\right|\right\}$. Analyses herein presented have been carried out by assuming $N = 3 \cdot 10^3$.

Appendix E. TPL-based flow in a cylindrical channel

For a cylindrical pipe (i.e., when $\theta = 0$, $R_{out} = R_{in} = R$, and $\chi = 1$, see Fig. 1) the comparison of the pressure gradient components in Eq. (A.3) leads to identify the radial term as identically null, so that $p = p(z)$. Moreover, due to Eqs. (A.5) and (B.9), it straightforward results that $p'(z)$ is a constant quantity, such that $p'(z) = -\Delta p/L$. As a consequence, the characteristic radii R_0 and R_∞ defined in Eqs. (21) are constant along the pipe axis, the axial velocity component v_z is constant with z, and the radial velocity component v_r is identically null. Accordingly, the analytical solution in Eqs. (22)–(28) reduces to

- $R \leq R_0$: one-region configuration (LSR; Fig. 3(a))

$$v_{z,LSR}(r) = \frac{\Delta p\,R^2}{4L\mu_0}\left[1 - \left(\frac{r}{R}\right)^2\right], \tag{E.1a}$$

Algorithm 1: Computation of the axial pressure gradient $p'(z)$ associated to the TPL-based solution provided by Eqs. (22) to (28) at discrete axial positions z_i, starting from $i = 1$ ($z_1 = 0$: inlet cross section) up to $i = N + 1$ ($z_{N+1} = L$: outlet cross section). As a notation rule, $p'_i = p'(z_i)$.

```
• $i = 1$ (inlet, $z_1 = 0$); $|p'_1|_{min} \equiv \min\left\{ \left|p'_{\mu_0}(z_1)\right| , \left|p'_{(K,n)}(z_1)\right| \right\}$
if $|p'_1|_{min}\, R_{in}/2 \le \tau_0$ then
    $p'_1 = p'_{\mu_0}(z_1)$
else if $\tau_0 < |p'_1|_{min}\, R_{in}/2 \le \tau_\infty$ then
    $p'_1 \;:\; Q_{LSR}(z_1) + Q_{MSR}(z_1) = Q$ with $p'_{1*} = -|p'_1|_{min}$
else if $|p'_1|_{min}\, R_{in}/2 > \tau_\infty$ then
    $p'_1 \;:\; Q_{LSR}(z_1) + Q_{MSR}(z_1) + Q_{HSR}(z_1) = Q$ with
     $p'_{1*} = -|p'_{\mu_\infty}(z_1)|$
end
• $i \neq 1$ (i.e., $0 = z_1 < z_i \le z_{N+1} = L$)
if $|p'_{i-1}|\, R(z_{i-1})/2 \le \tau_0$ then
    $p'_i = p'_{\mu_0}(z_i)$
    if $|p'_i|\, R(z_i)/2 > \tau_0$ then
        $p'_i \;:\; Q_{LSR}(z_i) + Q_{MSR}(z_i) = Q$ with $p'_{i*} = p'_{i-1}$
    end
else if $\tau_0 < |p'_{i-1}|\, R(z_{i-1})/2 \le \tau_\infty$ then
    $p'_i \;:\; Q_{LSR}(z_i) + Q_{MSR}(z_i) = Q$ with $p'_{i*} = p'_{i-1}$
    if $|p'_i|\, R(z_i)/2 > \tau_\infty$ then
        $p'_i \;:\; Q_{LSR}(z_i) + Q_{MSR}(z_i) + Q_{HSR}(z_i) = Q$ with $p'_{i*} = p'_{i-1}$
    end
else if $|p'_{i-1}|\, R(z_{i-1})/2 > \tau_\infty$ then
    $p'_i \;:\; Q_{LSR}(z_i) + Q_{MSR}(z_i) + Q_{HSR}(z_i) = Q$ with $p'_{i*} = p'_{i-1}$
end
```

$$\dot{\gamma}_{zr,LSR}(r) = -\frac{\Delta p}{2L\mu_0}\, r\,, \tag{E.1b}$$

$$Q = Q_{LSR} = \frac{\Delta p\, \pi R^4}{8L\mu_0}\,; \tag{E.1c}$$

- $R_0 < R \le R_\infty$: two-region configuration (LSR, MSR; Fig. 3(b))
  - For $r \le R_0$ (LSR regime):

$$v_{z,LSR}(r) = A_0 - \frac{\Delta p}{4L\mu_0} r^2\,, \tag{E.2a}$$

$$\dot{\gamma}_{zr,LSR}(r) = -\frac{\Delta p}{2L\mu_0}\, r\,, \tag{E.2b}$$

$$A_0 = \frac{1}{\alpha}\left(\frac{\Delta p}{2LK}\right)^{\frac{1}{n}} \left(R^\alpha - R_0^\alpha\right) + \frac{\Delta p\, R_0^2}{4L\mu_0}\,, \tag{E.2c}$$

$$Q_{LSR} = \pi R_0^2 \left(A_0 - \frac{\Delta p\, R_0^2}{8L\mu_0} \right)\,; \tag{E.2d}$$

  - For $R_0 < r \le R$ (MSR regime):

$$v_{z,MSR}(r) = \left(\frac{\Delta p}{2LK}\right)^{\frac{1}{n}} \frac{R^\alpha - r^\alpha}{\alpha}\,, \tag{E.3a}$$

$$\dot{\gamma}_{zr,MSR}(r) = -r^{\frac{1}{n}} \left(\frac{\Delta p}{2LK}\right)^{\frac{1}{n}}\,, \tag{E.3b}$$

$$Q_{MSR} = \frac{2\pi}{\alpha}\left(\frac{\Delta p}{2LK}\right)^{\frac{1}{n}} \left[\frac{R^\alpha}{2}\left(R^2 - R_0^2\right) - \frac{R^\beta - R_0^\beta}{\beta} \right]\,; \tag{E.3c}$$

$$Q = Q_{LSR} + Q_{MSR}\,; \tag{E.4}$$

- $R_\infty < R$: three-region configuration (LSR, MSR, HSR; Fig. 3(c))
  - For $r \le R_0$ (LSR regime):

$$v_{z,LSR}(r) = A_0 - \frac{\Delta p}{4L\mu_0} r^2\,, \tag{E.5a}$$

$$\dot{\gamma}_{zr,LSR}(r) = -\frac{\Delta p}{2L\mu_0}\, r\,, \tag{E.5b}$$

$$A_0 = \frac{1}{\alpha}\left(\frac{\Delta p}{2LK}\right)^{\frac{1}{n}} \left(R_\infty^\alpha - R_0^\alpha\right) + \frac{\Delta p}{4L}\left(\frac{R_0^2}{\mu_0} + \frac{R^2 - R_\infty^2}{\mu_\infty} \right)\,, \tag{E.5c}$$

$$Q_{LSR} = \pi R_0^2 \left(A_0 - \frac{\Delta p\, R_0^2}{8L\mu_0} \right)\,; \tag{E.5d}$$

  - For $R_0 < r \le R_\infty$ (MSR regime):

$$v_{z,MSR}(r) = -\frac{r^\alpha}{\alpha}\left(\frac{\Delta p}{2LK}\right)^{\frac{1}{n}} + A_1\,, \tag{E.6a}$$

$$\dot{\gamma}_{zr,MSR}(r) = -r^{\frac{1}{n}} \left(\frac{\Delta p}{2LK}\right)^{\frac{1}{n}}\,, \tag{E.6b}$$

$$A_1 = \frac{\Delta p}{4L\mu_\infty}\left(R^2 - R_\infty^2\right) + \frac{R_\infty^\alpha}{\alpha}\left(\frac{\Delta p}{2LK}\right)^{\frac{1}{n}}\,, \tag{E.6c}$$

$$Q_{MSR} = A_1 \pi \left(R_\infty^2 - R_0^2\right) - \frac{2\pi}{\alpha\beta}\left(\frac{\Delta p}{2LK}\right)^{\frac{1}{n}} \left(R_\infty^\beta - R_0^\beta\right)\,; \tag{E.6d}$$

  - For $R_\infty < r \le R$ (HSR regime):

$$v_{z,HSR}(r) = \frac{\Delta p}{4L\mu_\infty}\left(R^2 - r^2\right)\,, \tag{E.7a}$$

$$\dot{\gamma}_{zr,HSR}(r) = -\frac{\Delta p}{2L\mu_\infty}\, r\,, \tag{E.7b}$$

$$Q_{HSR} = \frac{\Delta p\, \pi}{8L\mu_\infty}\left(R^2 - R_\infty^2\right)^2\,; \tag{E.7c}$$

$$Q = Q_{LSR} + Q_{MSR} + Q_{HSR}\,; \tag{E.8}$$

where $\alpha = (n+1)/n$, and $\beta = (3n+1)/n$.

Appendix F. Supplementary material

The home-made MATLAB scripts used for the flow solution are available at https://github.com/SantesartiGEng/nonNewtoFlows.

Data availability

Data will be made available on request.

References

[1] R.B. Bird, R.C. Armstrong, O. Hassager, Dynamics of Polymeric Liquids. Vol. 1: Fluid mechanics, John Wiley and Sons Inc., New York, NY, 1987.

[2] J.F. Agassant, P. Avenas, P.J. Carreau, B. Vergnes, M. Vincent, Polymer Processing: Principles and Modeling, Carl Hanser Verlag GmbH Co KG, 2017.

[3] M.A. Rao, Rheology of Fluid and Semisolid Foods: Principles and Applications, Springer Science & Business Media, 2010.

[4] M. Conti, G. Santesarti, F. Scocozza, M. Marino, Models and simulations as enabling technologies for bioprinting process design, in: Bioprinting, Elsevier, 2022, pp. 137–206.

[5] M. Sarker, X. Chen, Modeling the flow behavior and flow rate of medium viscosity alginate for scaffold fabrication with a three-dimensional bioplotter, J. Manuf. Sci. Eng. 139 (8) (2017) 081002.

[6] N.S. Akbar, Blood flow analysis of Prandtl fluid model in tapered stenosed arteries, Ain Shams Eng. J. 5 (4) (2014) 1267–1275.
[7] P.K. Mandal, An unsteady analysis of non-Newtonian blood flow through tapered arteries with a stenosis, Int. J. Non-Linear Mech. 40 (1) (2005) 151–164.
[8] J.H. Forrester, D.F. Young, Flow through a converging-diverging tube and its implications in occlusive vascular disease—I: Theoretical development, J. Biomech. 3 (3) (1970) 297–305.
[9] H. Blasius, Laminare strömung in kanälen wechselnder breite, Z. Math. Phys. 58 (1910) 225–233.
[10] W. Langlois, Creeping viscous flow through a circular tube of nonuniform cross section, J. Appl. Mech. 39 (3) (1972) 657–660.
[11] W. Kotorynski, Viscous flow in axisymmetric pipes with slow variations, Comput. & Fluids 24 (6) (1995) 685–717.
[12] S. Sisavath, X. Jing, R.W. Zimmerman, Creeping flow through a pipe of varying radius, Phys. Fluids 13 (10) (2001) 2762–2772.
[13] A. Waele, Viscometry and Plastometry, Oil and Colour Chemists' Association, 1923.
[14] W. Ostwald, Ueber die geschwindigkeitsfunktion der viskosität disperser systeme. i, Kolloid-Zeitschrift 36 (2) (1925) 99–117.
[15] N. Casson, Rheology of disperse systems, Flow Equ. Pigment. Oil Suspens. Print. Ink Type. Rheol. Disperse Syst. (1959) 84–102.
[16] E.C. Bingham, Fluidity and Plasticity, McGraw-Hill, 1922.
[17] W.H. Herschel, R. Bulkley, Konsistenzmessungen von gummi-benzollösungen, Kolloid-Zeitschrift 39 (1926) 291–300.
[18] P.J. Carreau, Rheological equations from molecular network theories, Trans. Soc. Rheol. 16 (1) (1972) 99–127.
[19] K. Yasuda, Investigation of the Analogies Between Viscometric and Linear Viscoelastic Properties of Polystyrene Fluids (Ph.D. thesis), Massachusetts Institute of Technology, 1979.
[20] R.P. Chhabra, J.F. Richardson, Non-Newtonian Flow and Applied Rheology: Engineering Applications, Butterworth-Heinemann, 2011.
[21] V. Mazzanti, F. Mollica, N. El Kissi, Rheological and mechanical characterization of polypropylene-based wood plastic composites, Polym. Compos. 37 (12) (2016) 3460–3473.
[22] F.J. Gijsen, F.N. van de Vosse, J. Janssen, The influence of the non-Newtonian properties of blood on the flow in large arteries: steady flow in a carotid bifurcation model, J. Biomech. 32 (6) (1999) 601–608.
[23] B. Sauty, G. Santesarti, T. Fleischhammer, P. Lindner, A. Lavrentieva, I. Pepelanova, M. Marino, Enabling technologies for obtaining desired stiffness gradients in gelma hydrogels constructs, Macromol. Chem. Phys. 223 (2) (2022) 2100326.
[24] F. Chirianni, G. Vairo, M. Marino, Development of process design tools for extrusion-based bioprinting: From numerical simulations to nomograms through reduced-order modeling, Comput. Methods Appl. Mech. Engrg. 419 (2024) 116685.
[25] F. Chirianni, G. Vairo, M. Marino, Influence of extruder geometry and bio-ink type in extrusion-based bioprinting via an in silico design tool, Meccanica 59 (8) (2024) 1285–1299.
[26] S. Bair, A more complete description of the shear rheology of high-temperature, high-shear journal bearing lubrication, Tribol. Trans. 49 (1) (2006) 39–45.
[27] B.E. Meza, J.M. Peralta, S.E. Zorrilla, Effect of temperature and composition on rheological behaviour and sagging capacity of glaze materials for foods, Food Hydrocolloids 117 (2021) 106689.
[28] M.T. Gallagher, R.A. Wain, S. Dari, J.P. Whitty, D.J. Smith, Non-identifiability of parameters for a class of shear-thinning rheological models, with implications for haematological fluid dynamics, J. Biomech. 85 (2019) 230–238.
[29] G. Santesarti, M. Marino, F. Viola, R. Verzicco, G. Vairo, An insight into parameter identifiability issues in the Carreau-Yasuda model: A more consistent rheological formulation for shear-thinning non-Newtonian inelastic fluids, J. Non-Newton. Fluid Mech. (2025) 105438.
[30] J. Sutterby, Laminar converging flow of dilute polymer solutions in conical sections: Part I. Viscosity data, new viscosity model, tube flow solution, AIChE J. 12 (1) (1966) 63–68.
[31] S. Oka, T. Murata, Theory of the steady slow motion of non-Newtonian fluids through a tapered tube, Japan. J. Appl. Phys. 8 (1) (1969) 5.
[32] W.P. Walawender, P. Prasassarakich, Flow in tapering and cylindrical vessels, Microvasc. Res. 12 (1) (1976) 1–12.
[33] T. How, R. Black, D. Annis, Comparison of pressure losses in steady non-Newtonian flow through experimental tapered and cylindrical arterial prostheses, J. Biomed. Eng. 10 (3) (1988) 225–230.
[34] S. Priyadharshini, R. Ponalagusamy, et al., Biorheological model on flow of herschel-bulkley fluid through a tapered arterial stenosis with dilatation, Appl. Bionics Biomech. 2015 (2015).
[35] P. Panaseti, Y. Damianou, G.C. Georgiou, K.D. Housiadas, Pressure-driven flow of a Herschel-Bulkley fluid with pressure-dependent rheological parameters, Phys. Fluids 30 (3) (2018).
[36] L. Fusi, K.D. Housiadas, G.C. Georgiou, Flow of a bingham fluid in a pipe of variable radius, J. Non-Newton. Fluid Mech. 285 (2020) 104393.
[37] A. Lavrov, Flow of truncated power-law fluid between parallel walls for hydraulic fracturing applications, J. Non-Newton. Fluid Mech. 223 (2015) 141–146.
[38] M. Wrobel, On the application of simplified rheological models of fluid in the hydraulic fracture problems, Internat. J. Engrg. Sci. 150 (2020) 103275.
[39] G. Felisa, A. Lenci, I. Lauriola, S. Longo, V. Di Federico, Flow of truncated power-law fluid in fracture channels of variable aperture, Adv. Water Resour. 122 (2018) 317–327.
[40] M. Li, X. Tian, J.A. Kozinski, X. Chen, D.K. Hwang, Modeling mechanical cell damage in the bioprinting process employing a conical needle, J. Mech. Med. Biology 15 (05) (2015) 1550073.
[41] E. Reina-Romo, S. Mandal, P. Amorim, V. Bloemen, E. Ferraris, L. Geris, Towards the experimentally-informed in silico nozzle design optimization for extrusion-based bioprinting of shear-thinning hydrogels, Front. Bioeng. Biotechnol. 9 (2021) 701778.
[42] R. Chand, B.S. Muhire, S. Vijayavenkataraman, Computational fluid dynamics assessment of the effect of bioprinting parameters in extrusion bioprinting, Int. J. Bioprinting 8 (2) (2022).
[43] J. Leppiniemi, P. Lahtinen, A. Paajanen, R. Mahlberg, S. Metsa-Kortelainen, T. Pinomaa, H. Pajari, I. Vikholm-Lundin, P. Pursula, V.P. Hytonen, 3D-printable bioactivated nanocellulose–alginate hydrogels, ACS Appl. Mater. Interfaces 9 (26) (2017) 21959–21970.
[44] L. Ning, N. Betancourt, D.J. Schreyer, X. Chen, Characterization of cell damage and proliferative ability during and after bioprinting, ACS Biomater. Sci. Eng. 4 (11) (2018) 3906–3918.
[45] F. Irgens, Rheology and Non-Newtonian Fluids, vol. 190, Springer, 2014.
[46] M. Itskov, et al., Tensor Algebra and Tensor Analysis for Engineers, Springer, 2007.
[47] J. Bear, Dynamics of Fluids in Porous Media, Courier Corporation, 2013.
[48] I.T. Ozbolat, M. Hospodiuk, Current advances and future perspectives in extrusion-based bioprinting, Biomaterials 76 (2016) 321–343.
[49] N. Paxton, W. Smolan, T. Böck, F. Melchels, J. Groll, T. Jungst, Proposal to assess printability of bioinks for extrusion-based bioprinting and evaluation of rheological properties governing bioprintability, Biofabrication 9 (4) (2017) 044107.
[50] E.A. Kiyotake, A.W. Douglas, E.E. Thomas, S.L. Nimmo, M.S. Detamore, Development and quantitative characterization of the precursor rheology of hyaluronic acid hydrogels for bioprinting, Acta Biomater. 95 (2019) 176–187.
[51] D. Dodge, A. Metzner, Turbulent flow of non-Newtonian systems, AIChE J. 5 (2) (1959) 189–204.
[52] J.A. Tichy, The effect of fluid inertia in hydrodynamic lubrication studied by a linearization method: Two useful applications, Internat. J. Engrg. Sci. 24 (10) (1986) 1607–1613.
[53] R. Malvano, F. Vatta, The influence of fluid inertia in steady laminar lubrication, J. Lubr. Technol. 105 (1) (1983) 77–83.
[54] ANSYS FLUENT - Theory guide - Solver theory, 2025, https://www.afs.enea.it/project/neptunius/docs/fluent/html/th/node359.htm. (Accessed 20 December 2025).
[55] ANSYS FLUENT - User guide - Physical properties: viscosity, 2025, https://www.afs.enea.it/project/neptunius/docs/fluent/html/ug/node292.htm. (Accessed 20 December 2025).
[56] A. Rodríguez de Castro, G. Radilla, Flow of yield stress and c arreau fluids through rough-walled rock fractures: Prediction and experiments, Water Resour. Res. 53 (7) (2017) 6197–6217.
[57] A. Lavrov, Flow of non-Newtonian fluids in single fractures and fracture networks: Current status, challenges, and knowledge gaps, Eng. Geol. 321 (2023) 107166.
[58] T. Sochi, Analytical solutions for the flow of carreau and cross fluids in circular pipes and thin slits, Rheol. Acta 54 (2015) 745–756.
[59] S.K. Kim, Flow-rate based method for velocity of fully developed laminar flow in tubes, J. Rheol. 62 (6) (2018) 1397–1407.
[60] A. Daly, M. Prendergast, A. Hughes, J. Burdick, Bioprinting for the biologist, Cell 184 (2021) 18–32.
[61] R. Chang, J. Nam, W. Sun, Effects of dispensing pressure and nozzle diameter on cell survival from solid freeform fabrication–based direct cell writing, Tissue Eng. Part A 14 (2008) 41–48.
[62] M. Li, X. Tian, D. Schreyer, X. Chen, Effect of needle geometry on flow rate and cell damage in the dispensing-based biofabrication process, Biotechnol. Prog. 27 (2011) 1777–1784.
[63] S. Han, C. Kim, S. Jin, T. Kim, Study of the process-induced cell damage in forced extrusion bioprinting, Biofabrication 13 (2021) 035048.
[64] K. Nair, M. Gandhi, S. Khalil, K.C. Yan, M. Marcolongo, K. Barbee, W. Sun, Characterization of cell viability during bioprinting processes, Biotechnol. J.: Heal. Nutr. Technol. 4 (8) (2009) 1168–1177.
[65] D. Katritsis, L. Kaiktsis, A. Chaniotis, J. Pantos, E.P. Efstathopoulos, V. Marmarelis, Wall shear stress: theoretical considerations and methods of measurement, Prog. Cardiovasc. Dis. 49 (5) (2007) 307–329.
[66] E. Cecchi, C. Giglioli, S. Valente, C. Lazzeri, G.F. Gensini, R. Abbate, L. Mannini, Role of hemodynamic shear stress in cardiovascular disease, Atherosclerosis 214 (2) (2011) 249–256.

[67] S. Boularaoui, G. Al Hussein, K.A. Khan, N. Christoforou, C. Stefanini, An overview of extrusion-based bioprinting with a focus on induced shear stress and its effect on cell viability, Bioprinting 20 (2020) e00093.

[68] J. Shi, B. Wu, S. Li, J. Song, B. Song, W.F. Lu, Shear stress analysis and its effects on cell viability and cell proliferation in drop-on-demand bioprinting, Biomed. Phys. Eng. Express 4 (4) (2018) 045028.

[69] P. Gaziano, M. Marino, Computational modeling of cell motility and clusters formation in enzyme-sensitive hydrogels, Meccanica 59 (2024) 1335–1349.

[70] P. Gaziano, M. Marino, A phase-field model of cell motility in biodegradable hydrogel scaffolds for tissue engineering applications, Comput. Mech. 74 (2024) 45–66.

[71] M. Gieriig, P. Gaziano, P. Wriggers, M. Marino, Post-angioplasty remodeling of coronary arteries investigated via a chemo-mechano-biological in silico model, J. Biomech. 166 (2024) 112058.

[72] R. Liu, Q. Liu, Non-modal instability in plane couette flow of a power-law fluid, J. Fluid Mech. 676 (2011) 145–171.

[73] B. Khomami, Interfacial stability and deformation of two stratified power law fluids in plane poiseuille flow part I. Stability analysis, J. Non-Newton. Fluid Mech. 36 (1990) 289–303.

[74] J. Kim, P.K. Singh, J.B. Freund, R.H. Ewoldt, Uncertainty propagation in simulation predictions of generalized Newtonian fluid flows, J. Non-Newton. Fluid Mech. 271 (2019) 104138.

[75] M. Rahimnejad, T. Labonte-Dupuis, N.R. Demarquette, S. Lerouge, A rheological approach to assess the printability of thermosensitive chitosan-based biomaterial inks, Biomed. Mater. 16 (1) (2020) 015003.